HHS Public Access

Author manuscript

Nat Immunol. Author manuscript; available in PMC 2019 February 20.

Published in final edited form as:

Nat Immunol. 2018 September ; 19(9): 986–1000. doi:10.1038/s41590-018-0182-3.

Hyperactivated PI3Kδ promotes self and commensal reactivity at the expense of optimal humoral immunity

Silvia Preite[1,2,*], **Jennifer L. Cannons**[1,2,^], **Andrea J. Radtke**[2,^], **Ivan Vujkovic-Cvijin**[3,^], **Julio Gomez-Rodriguez**[1,2], **Stefano Volpi**[4,5], **Bonnie Huang**[1,2], **Jun Cheng**[1], **Nicholas Collins**[3], **Julie Reilley**[1,2], **Robin Handon**[1], **Kerry Dobbs**[6], **Lutfi Huq**[3], **Indu Raman**[7], **Chengsong Zhu**[7], **Quan-Zhen Li**[7,8], **Ming O. Li**[9], **Stefania Pittaluga**[10], **Gulbu Uzel**[6], **Luigi D. Notarangelo**[6], **Yasmine Belkaid**[3,11], **Ronald N. Germain**[2], and **Pamela L. Schwartzberg**[1,2,*]

[1]National Human Genome Research Institute, National Institutes of Health, Bethesda, MD, USA.

[2]Laboratory of Immune System Biology, National Institute of Allergy and Infectious Diseases National Institutes of Health, Bethesda, MD, USA.

[3]Laboratory of Parasitic Diseases, National Institute of Allergy and Infectious Diseases, National Institutes of Health, Bethesda, MD, USA.

[4]Clinica Pediatrica e Reumatologia, Centro per le Malattie Autoinfiammatorie e Immunodeficienze, Istituto Giannina Gaslini Genoa, Italy.

[5]Università degli Studi di Genova, Genoa, Italy.

[6]Laboratory of Clinical Immunology and Microbiology, National Institute of Allergy and Infectious Diseases. National Institutes of Health, Bethesda, MD, USA.

[7]Microarray Core Facility, University of Texas Southwestern Medical Center, Dallas, TX, USA.

[8]Department of Immunology, University of Texas Southwestern Medical Center, Dallas, TX, USA.

[9]Immunology Program, Memorial Sloan-Kettering Cancer Center, New York, New York, USA.

[10]Laboratory of Pathology, National Cancer Institute, National Institutes of Health, Bethesda, MD, USA.

[*]Corresponding authors: Pamela L. Schwartzberg (pams@mail.nih.gov), Silvia Preite (silvia.preite@nih.gov).

Author contributions

S.Pr. designed and performed experiments, analyzed and interpreted data, and wrote the manuscript; J.L.C., A.J.R., I.V.-C. equally contributed to this work and are listed alphabetically. J.L.C. generated the *Pik3cd*$^{E1020K/+}$ mouse model, conceived the initial idea of the project, designed and performed experiments and provided helpful discussions. A.J.R. designed, performed and analyzed immunohistochemistry and confocal microscopy experiments. I.V.-C. designed, performed and analyzed gut and microbiome experiments. J.G.-R. generated the *Pik3cd*$^{E1020K/+}$ mouse model and provided helpful discussions. S.V. and K.D. analyzed auto-antibody arrays. B.H. helped with experiments and provided helpful discussions. J.C. performed ES cell manipulations and injections. N.C. and L.H. assisted with gut and microbiome experiments. J.R. and R.H. provided technical support. I.R. and C.Z. helped generate and analyze autoantibody array data. Q.-Z.L. designed the array and analyzed the data. M.O.L. provided *Rosa26*- HA-hFoxo1^{AAA} mice. S.Pi. provided experimental advice. G.U. provided patient samples and helpful discussions. L.D.N., Y.B., R.N.G. provided vital reagents and intellectual input. P.L.S. conceived the project, wrote the manuscript, and provided overall direction of the study.

[^]shared second authors, in alphabetical order.

Accession codes. Accession codes for microbiome sequences are publically available at: (https://www.ncbi.nlm.nih.gov/Traces/study/?acc=SRP132959).

Competing interests

The authors declare no competing interests.

[11]Microbiome Program, National Institute of Allergy and Infectious Diseases. National Institutes of Health, Bethesda, MD, USA.

Abstract

Gain-of-function mutations in phosphoinositide 3-kinase p110δ (PI3Kδ) result in a human primary immunodeficiency characterized by lymphoproliferation, respiratory infections and inefficient vaccine responses. However, what promotes these immune disturbances at the cellular and molecular level remains unknown. We describe a mouse model that recapitulates major features of this disease and use this model and patient samples to probe how hyperactive PI3Kδ fosters aberrant humoral immunity. We found that mutant PI3Kδ led to ICOS-independent increases in T follicular helper (T_{FH}) and germinal center (GC) B cells, disorganized GCs, and poor class-switched antigen-specific responses to immunization, associated with altered regulation of FOXO1 and BCL-2 family members. Notably, aberrant responses were accompanied by increased reactivity to gut bacteria, and a broad increase in autoantibodies that were dependent on commensal microbial stimulation. Our findings suggest that proper PI3Kδ regulation is critical for ensuring optimal host-protective humoral immunity despite tonic stimulation from the commensal microbiome.

Introduction

p110δ, a catalytic subunit of phosphoinositide 3-kinase (PI3K) expressed primarily in hematopoietic cells, is activated by cytokine, antigen and costimulatory receptors, and coordinates signaling involved in T and B cell activation and differentiation[1]. Patients with gain-of-function point-mutations in p110δ exhibit a primary immunodeficiency called PASLI (p110δ-activating mutation causing senescent T cells, lymphadenopathy and immunodeficiency) or APDS (activated-PI3Kδ syndrome), characterized by lymphopenia, lymphoproliferation, recurrent respiratory infections and mucosal lymphoid follicles. Patients display increased effector and reduced naïve T cells, enlarged germinal centers (GCs), fewer class-switched memory B cells, and impaired antibody responses to vaccination[2–4]. However, cellular and molecular events contributing to these phenotypes remain to be characterized.

Clues to how altered PI3Kδ activity might disrupt antibody responses come from work demonstrating that T and B cells intimately co-operate in antigen-driven antibody responses via generation of GCs, specialized microenvironments for immunoglobulin class switching, affinity maturation, and development of memory B and long-lived plasma cells[5]. GCs also help maintain tolerance through elimination of self-reactive clones[6]. $CD4^+$ T follicular helper (T_{FH}) cells provide essential signals for GC formation and maintenance, as well as for survival and selection of B cells producing high-affinity antibodies[7,8] and deletion of potentially auto-reactive B cells[9]. T_{FH} cells express the chemokine receptor CXCR5, inhibitory receptor PD-1, costimulatory molecule ICOS and transcription factor BCL-6[10]. In activated T cells, ICOS potently activates PI3Kδ, leading to inactivation of FOXO1, a transcriptional repressor of *Bcl6*[11,12]. In B cells, PI3Kδ is critical for survival, proliferation and differentiation, via integration of signals from the B cell antigen-receptor (BCR), CD19,

BAFF-R, CD40, cytokines and Toll-like-receptors (TLRs)[13]. Notably, mice with abrogated PI3Kδ activity have defective T_{FH} and GC formation[14,15], demonstrating important roles for PI3Kδ in GC reactions. Furthermore, a proportion of PASLI/APDS patients display autoantibodies and autoimmune-mediated organ damage[4,16], suggesting that regulation of PI3Kδ activity is also important for limiting self-reactivity. These findings raise the possibility that GCs may be a major site of aberrant behavior by lymphocytes expressing mutant PI3Kδ.

Here, we report a mouse model of PASLI/APDS (*Pik3cd*$^{E1020K/+}$ mice) and use this model to study how overactive PI3Kδ affects humoral responses, focusing on GCs. We found that PI3Kδ^{E1020K} led to exaggerated production of T_{FH} cells and GCs, associated with lymphocyte hypereactivity, altered regulation of FOXO1 and BCL-2 family member and increased B cell survival. Nonetheless, *Pik3cd*$^{E1020K/+}$ mice displayed a diminished capacity for robust class-switched antigen-specific antibodies to immunization, despite augmented anti-self and anti-commensal responses. Importantly, antibiotic treatment of *Pik3cd*$^{E1020K/+}$ mice revealed a requirement for commensal stimulation in the generation of hyperactivated immunophenotypes. Our results suggest that tight regulation of PI3Kδ activity is critical to constrain tonic activation induced by the commensal microbiome while facilitating protective immune responses.

Results

PASLI/APDS patients display increased blood T_{FH} cells

Circulating T_{FH} (cT_{FH}) cells are increased after immunization and in autoimmune conditions and reflect bona fide T_{FH} cells residing in secondary lymphoid organs[17]. Despite impaired antigen-specific responses to vaccination[2,3], we found increased frequencies of $CD4^+CD45RA^-CD25^-CXCR5^+$ cT_{FH} cells in PASLI/APDS patients compared to healthy donors (HD) (Fig. 1a). Patient cT_{FH} cells also exhibited elevated PD-1 (Fig. 1b), which is associated with enhanced effector phenotypes and ongoing GC reactions[18]. Furthermore, patients exhibited increased percentages of $CXCR3^+$ T_{FH} cells (Fig. 1c), consistent with a bias towards $T_{FH}1$ cells, which do not effectively help naive B cells *in vitro*[17]. Thus, PASLI/APDS patients show altered homeostasis of effector $CD4^+$ T cell populations that influence humoral responses.

Pik3cd$^{E1020K/+}$ mice recapitulate features of PASLI/APDS

To explore the impact of hyperactivated PI3Kδ on immune responses, we generated a mouse model expressing p110δ^{E1020K}, corresponding to the most common gain-of-function mutant (E1021K) in PASLI/APDS patients[2,4] (Supplementary Fig. 1a). Heterozygous *Pik3cd*$^{E1020K/+}$ mice recapitulated many features of PASLI/APDS, including reduced circulating white blood cells (Fig. 2a), lymphadenopathy (Supplementary Fig. 1b) and increased splenic cellularity (Fig. 2b)[2,4].

The most common clinical phenotype of PASLI/APDS patients is recurrent respiratory infections, often associated with lung and tracheal mucosal nodules[4,16]. Additionally, ~30% of the patients display enteropathy with gastrointestinal nodular mucosal lymphoid

hyperplasia[4,16]. We found evidence of similar perivascular and peribronchiolar lymphoid aggregates in the lungs (Fig. 2c, left), and increased isolated lymphoid follicles (ILFs) in the small intestines of mutant mice (Fig. 2c, right). These similarities suggest that *Pik3cd*$^{E1020K/+}$ mice provide a useful tool to dissect cellular and molecular mechanisms contributing to the human disease.

To evaluate how PI3Kδ specifically affects lymphocytes, we examined T- and B-cell populations. Despite comparable frequencies of CD4$^+$ T cells, we found reduced naïve and increased activated CD4$^+$ T cell percentages in spleens and peripheral lymph nodes (pLN) of mutant mice (Fig. 2d and Supplementary Table 1), similar to patients' blood[2,4]. These phenotypes became more pronounced over time (Supplementary Table 1); by one year of age, *Pik3cd*$^{E1020K/+}$ mice had virtually no CD62L$^+$CD44^{lo} naïve CD4$^+$ T cells (Supplementary Fig. 1c).

A partial block of B cell development is seen in PASLI/APDS patients, with increased circulating transitional CD20$^+$CD10$^+$ B cells[4,19]. Although frequencies of splenic B cells were comparable to wild-type (Supplementary Table 1), mutant mice had higher numbers and altered populations of CD93$^+$ transitional B cells, including more T1 cells, consistent with a partial developmental block (Supplementary Fig. 1d). Additionally, mutant mice had altered expression of surface-IgM and IgD, reduced follicular (FO), and expanded marginal zone (MZ) B cells (Supplementary Fig. 1e,f), supporting a role for PI3Kδ in driving MZ B cell differentiation[20]. Finally, mutant mice exhibited increased peritoneal B-1a B cells (Supplementary Fig. 1g,h), a self-reactive/innate-like population[21]. Therefore, *Pik3cd*$^{E1020K/+}$ mice develop T and B cells, but exhibit alterations in lymphocyte activation and homeostasis, as seen in patients.

Elevated lymphocyte activation in *Pik3cd*$^{E1020K/+}$ mice

Consistent with observations in patients' blood, we found increased PD-1$^+$CXCR5$^+$CD4$^+$ T cells in the spleens of *Pik3cd*$^{E1020K/+}$ mice (Fig. 2e). These included both Foxp3$^-$ T_{FH} and Foxp3$^+$ regulatory T follicular helper (T_{FR}) cells (Fig. 2f), yet the T_{FH}:T_{FR} ratio remained comparable to wild-type (Supplementary Table 1). Both BCL-6^{lo} pre-T_{FH} and BCL-6^{hi} GC-T_{FH} cells were expanded (Supplementary Fig. 2a). Furthermore, although 2-month-old mutant mice exhibited relatively normal pLN T_{FH} cell numbers, the percentage and number of these cells increased in both LNs and spleens as mice aged (Supplementary Fig. 2b and Supplementary Table 1). By one year, the majority of CD4$^+$ T cells expressed abundant PD-1, ICOS and CXCR5 (Supplementary Fig. 2c).

In parallel, we detected marked increases in GC B cells in both LNs and spleens, as well as splenic CD138$^+$ plasma cells in mutant mice (Fig. 2g,h and Supplementary Fig. 2d). Consistent with time-dependent increases in lymphocyte activation, these phenotypes became more pronounced with age, together with a reduction of IgD$^+$ naïve B cells (Supplementary Fig. 2d,e and Supplementary Table 1). Accordingly, we observed increased serum IgM and IgG in mutant mice (Fig. 2i). Elevated serum IgM is also seen in PASLI/APDS patients, although IgG concentrations are variable[2–4]. Thus, like patients, *Pik3cd*$^{E1020K/+}$ mice display expanded activated lymphocyte populations associated with increased antibody production.

Defective T-dependent humoral responses

To explore the effect of activated PI3Kδ on antigen-induced humoral responses, we immunized mice subcutaneously with the T-dependent antigen, 4-Hydroxy-3-nitrophenylacetyl-ovalbumin (NP-OVA) in alum. Mice were immunized at 2 months, when the frequency of T_{FH} cells was relatively normal, or at 4 months of age, when mutant mice exhibited increased T_{FH} and GC B cells, similar to the patients. As expected after immunization, T_{FH} and GC B cells expanded in the draining LN (dLN) compared to the resting LN (rLN) in both age groups of wild-type mice (Fig. 3a and Supplementary Fig. 3a). Similarly, T_{FH} and GC B cells increased after immunization in young (2-month-old) mutant mice (Supplementary Fig. 3a). In contrast, immunization did not increase the frequency of T_{FH} and GC B cells in the dLN of 4-month-old mutant mice (Fig. 3a). Furthermore, while mutant baseline rLNs had greater cellularity than wild-type rLNs, after immunization, mutant dLNs had comparable, or even lower cell numbers, than wild-type dLNs (Supplementary Fig. 3b).

Despite increased frequencies of GC B cells in mutant mice, the percentages and numbers of antigen-binding (NP^+) GC B cells were lower, so that the ratio of NP^+ antigen-specific to NP^-GC B cells were substantially reduced in these animals (Fig. 3b,c and Supplementary Fig. 3c). MFIs of NP-binding cells were also lower, which may reflect lower surface BCR levels on mutant cells (Fig. 3b). These phenotypes became even pronounced by 1 year of age, when many mutant mice had very few NP-specific GC B cells post-immunization (Supplementary Fig. 3d). However, decreased ratios of NP^+ to NP^- GC B cells were also observed in 2-month-old mutant mice (Supplementary Fig. 3e), suggesting that these observations were not solely the result of increased GCs preventing new antigen-specific responses. Within the NP^+ GC B cell compartment, we found reduced percentages of $IgG1^+$ cells, indicating impaired class switching in mutant mice (Fig. 3d).

Analyses of serum antibody concentrations revealed a wide range of NP-specific IgM in *Pik3cd*$^{E1020K/+}$ mice that overlapped with that seen in wild-type (Fig. 3e). However, consistent with impaired class-switching, NP-specific IgG1 was significantly reduced (Fig. 3f), despite mutant mice having higher total serum IgG1, likely as a result of increased activated B and plasma cells (Supplementary Fig. 3f). Nonetheless, ratios between serum high-affinity anti-NP_4 and total anti-NP_{20} antibodies, which are often used to evaluate affinity maturation[22], were comparable between wild-type and mutants (Fig. 3f). Thus, *Pik3cd*$^{E1020K/+}$ mice exhibited marked alterations in humoral immunity, characterized by increased basal GC formation, but defects in the magnitude of class-switched antigen-specific antibody responses.

Hyperactivated-PI3Kδ results in disorganized GCs

To provide further insight into the nature of these defects, we used high-dimensional immunofluorescence confocal microscopy to evaluate the structure and organization of GCs (Fig. 3g). To model the immune activation observed in patients, 4-month-old mice were evaluated, both at steady state and after immunization. In line with our flow analyses, wild-type rLNs had very few, poorly-formed GCs within the follicular dendritic cell (FDC) networks (Fig. 3g, I); however, post-immunization, we observed increased generation of

GCs, as marked by BCL-6$^+$ cells in the dLN (Fig. 3g, II). In marked contrast, the rLNs of mutant mice already had expanded GC areas that filled the FDC networks (Fig. 3g, III). Collectively, almost all FDC areas were occupied with BCL-6$^+$ GCs in the dLN of both wild-type and mutants, but strikingly also in rLN of mutant mice (Supplementary Fig. 3g).

Enlargement of a representative wild-type GC permitted the identification of the dark zone (DZ), which was enriched with highly-packed BCL-6$^+$ GC B cells, and the light zone (LZ), which was demarcated by CD35$^+$ FDCs and included the bulk of PD-1$^+$CD4$^+$ T_{FH} cells (Fig. 3g, II, middle and bottom). Although sizes of mutant dLN GCs were variable (Supplementary Fig. 3h), mutant GCs from both rLN and dLN showed altered organization with increased T_{FH} cells invading the DZ (Fig. 3g, III-IV, middle and bottom). These findings were confirmed by histo-cytometric analyses quantitating T_{FH} cells per DZ area (Supplementary Fig. 3i-k). Flow cytometry further showed a reduction of DZ, and increase in LZ NP$^+$ GC B cells in mutants, as identified by CXCR4 and CD86 expression[23] (Supplementary Fig. 3l). Increased percentages of Foxp3$^+$ regulatory T (T_{reg}) and T_{FR} cells were also observed in mutant mice (Fig. 3g, III-IV), as confirmed by flow cytometry (Supplementary Fig. 3m); however, T_{FR} cells were seen at the T/B cell border and within the B cell follicles in both wild-type and mutants, consistent with a recent study[24]. Thus, *Pik3cd*$^{E1020K/+}$ mice exhibit disorganized GCs with extensive T_{FH} cell infiltration in the DZ and poor demarcation of LZ and DZ areas, indicative of a dysregulated immune response.

Increased T_{FH} cell differentiation is T cell intrinsic

The formation of GCs involves intimate interactions and crosstalk between both antigen-specific T_{FH} and B cells. To probe distinct cellular contributions to these altered humoral phenotypes, we transferred naïve wild-type or mutant OVA-specific TCR-transgenic OT-II cells into wild-type hosts, which were then immunized i.p. with NP-OVA (Fig. 4a). Eight days post-immunization, wild-type and mutant OT-II cells had expanded comparably (Fig. 4b) and were homogeneously CD44^{hi} (Supplementary Fig. 4a). However, a higher percentage of the mutant OT-II cells acquired T_{FH} cell markers, (Fig. 4c), including markers of both pre-T_{FH} and GC-T_{FH} cells (Supplementary Fig. 4b). Notably, *Pik3cd*$^{E1020K/+}$ T_{FH} cells produced interleukin 21 (IL-21) and provided *in vitro* B cell help similar to their wild-type counterparts (Supplementary Fig. 4c,d), consistent with normal function. Thus, *Pik3cd*$^{E1020K/+}$ drives a cell-intrinsic expansion of T_{FH} cells.

ICOS-independent generation of T_{FH} cells

ICOS is a critical receptor that activates PI3Kδ and is essential for T_{FH} cell differentiation[15]. Since p110δ^{E1020K} is constitutively active, we hypothesized it may bypass requirements for ICOS:ICOS-L interactions for T_{FH} cell development. To test this, we transferred naïve wild-type or mutant OT-II cells into wild-type mice, which were then immunized and treated with a blocking-antibody for ICOS-L (Fig. 4d). Anti-ICOS-L treatment decreased wild-type OT-II T_{FH} cells, but failed to effectively block mutant OT-II T_{FH} cell differentiation (Fig. 4e), despite reducing endogenous wild-type T_{FH} cells in the same mice (Supplementary Fig. 4e). Furthermore, although anti-ICOS-L treatment reduced both T_{FH} and GC B cells in intact wild-type mice, neither population was abrogated in the mutants (Supplementary Fig. 4f-h).

Thus, activated PI3Kδ overcame requirements for ICOS-ICOS-L interaction for T_{FH} cell differentiation and maintenance.

In vitro stimulation of naive OT-II cells with $OVA_{232–339}$ revealed augmented induction of activation markers on mutant cells, suggesting an increased sensitivity to stimulation (Supplementary Fig. 4i). Similarly, we observed enhanced PI3Kδ-dependent TCR plus CD28-induced phosphorylation of AKT and S6, two downstream readouts of PI3K activity, as seen in patients' cells[2–4] (Fig. 4f). Activated p-AKT phosphorylates FOXO transcription factors, leading to their sequestration outside of the nucleus and subsequent degradation[25]. Intriguingly, in the absence of FOXO1, T_{FH} cells are also generated independently of ICOS[11]. To evaluate FOXO1, T cells were activated *in vitro* to induce ICOS expression, rested, and restimulated with anti-ICOS. After activation *in vitro*, wild-type $CD4^+$ T cells showed a clear population of cells staining for p-FOXO1, which increased further upon ICOS restimulation (Fig. 4g). In contrast, *Pik3cd*$^{E1020K/+}$ T cells exhibited abundant p-FOXO1 even prior to ICOS restimulation (Fig. 4g). Furthermore, expression of $FOXO1^{AAA}$, an AKT-resistant mutant of FOXO1[26], decreased percentages of mutant T_{FH} cells generated *in vivo* to levels similar to wild-type (Fig. 4h), in addition to reducing overall T cell accumulation, as previously reported[11] (data not shown). Thus, expression of activated PI3Kδ bypassed the need for ICOS to phosphorylate and inactivate FOXO1, an inhibitor of T_{FH} cell differentiation.

Increased GC B and plasma cells, yet reduced antigen-specific responses

Despite increased T_{FH} cell differentiation, transfer of *Pik3cd*$^{E1020K/+}$ OT-II cells into wild-type hosts was not sufficient to generate greater numbers of GC B cells, at least within the time frame examined (Supplementary Fig. 4j). To investigate B cell-intrinsic roles of activated PI3Kδ, we transferred naïve wild-type and *Pik3cd*$^{E1020K/+}$ Hen-egg-lysozyme (HEL)-specific BCR transgenic MD4 B cells, together with naïve wild-type OT-II cells, into wild-type mice which were then immunized with HEL-$OVA_{323–339}$ (Fig. 5a)[22]. Eight days post immunization, wild-type OT-II cells behaved similarly in the presence of either wild-type or mutant MD4 B cells (Supplementary Fig. 5a). However, mutant MD4 B cells expanded more (Fig. 5b), and displayed greater differentiation into GC B cells compared to wild-type MD4 B cells (Fig. 5c), demonstrating cell-intrinsic phenotypes.

To evaluate antigen-specific responses, we transferred wild-type or *Pik3cd*$^{E1020K/+}$ naïve polyclonal B cells, together with naive wild-type OT-II cells, into MD4 wild-type hosts which were then immunized with NP-OVA (Supplementary Fig. 5b). In this setting, only the transferred polyclonal B cells can respond to the immunogen. Again, we observed increased expansion of mutant B cells (Supplementary Fig. 5c), as well as increased numbers of GC B cells and splenic plasma cells (Supplementary Fig. 5d,e). Nonetheless, the percentage of NP^+ GC B cells, as well as the ratios between numbers of NP^+ and $NP^—$ GC B cells were reduced for the transferred mutant B cells (Supplementary Fig. 5f).

In vitro stimulation of mutant follicular MD4-B cells with HEL revealed heightened induction of activation markers, suggesting lower thresholds of activation (Supplementary Fig. 5g). We also observed higher proliferation and BrdU incorporation in mutant follicular B cells in response to multiple stimuli *in vitro*, consistent with B cell-intrinsic effects of

PI3Kδ^{E1020K} (Fig. 5d,e). Additionally, *in vitro* activation of mutant B cells led to increased plasma cell differentiation (Fig 5f, left and Supplementary Fig. 5h), and reduced IgG1 switching (Fig 5f, right), both of which occurred primarily in cells that had undergone extensive proliferation, as in wild-type cultures. These phenotypes paralleled findings *in vivo* and could be reversed by a selective PI3Kδ inhibitor (Fig. 5g). Together, these data argue that PI3Kδ^{E1020K} causes B cell intrinsic increases in GC B and plasma cell outgrowth, yet impaired B cell capacity for class-switched antigen-specific responses.

PI3Kδ^{E1020K} results in reduced GC B cell death

In GCs, B cells undergo high rates of cell death, resulting in the culling of low-affinity and non-antigen-specific B cells that is required to generate proper antigen-specific antibody responses[6]. In contrast, *ex vivo Pik3cd*$^{E1020K/+}$ GC B cells exhibited increased percentages of live GC B cells, and decreased cells staining for activated caspase-3 compared to wild-type (Fig. 5h,i). This increased survival appeared to be B-cell intrinsic, as mixed-bone marrow chimeras of wild-type and mutant cells revealed increased percentages of GC B cells, as well as live cells within the mutant GC B cell compartment (Supplementary Fig. 5i,j). Although differences in *in vitro* steady state survival of unstimulated naïve follicular B cells were not observed (Supplementary Fig. 5k), multiple stimuli, including anti-IgM and lipopolysaccharide (LPS), increased the percentages of live mutant proliferating cells (Supplementary Fig. 5l). Moreover, IL-4 increased mutant B cell survival relative to wild-type, even in the absence of proliferation (Supplementary Fig. 5m). In contrast, BAFF did not increase survival in the mutant, but consistently led to B cell proliferation, which was not observed in wild-type cells (Supplementary Fig. 5m). Treatment with a selective PI3Kδ inhibitor reduced both B cell proliferation and viability *in vitro* (Supplementary Fig. 5n), directly implicating activated PI3Kδ in these phenotypes. Thus, PI3Kδ^{E1020K} both increased survival and proliferation of activated B cells.

FOXO proteins transcriptionally activate pro-apoptotic genes such as *Bcl2l11*, encoding the BCL-2 family member BIM[27]. As in T cells, we observed increased phosphorylation of AKT and S6 (Fig. 5j), as well as a higher percentage of p-FOXO1^{+} *Pik3cd*$^{E1020K/+}$ B cells following *in vitro* stimulation (Fig. 5k). Consistent with these observations, mutant GC B cells exhibited reduced *Bcl2l11* expression (Fig. 5l). AKT-mediated phosphorylation also inhibits GSK3β which targets the anti-apoptotic BCL-2 family member, MCL-1, for proteasome degradation[28]. Accordingly, *in vitro* stimulation revealed augmented MCL-1 expression in mutant B cells (Fig. 5m). Thus, activated PI3Kδ regulates multiple pathways that promote B cell survival.

Pik3cd$^{E1020K/+}$ mice display elevated serum autoantibodies

The induction of B-cell apoptosis within the GC is essential for maintaining self-tolerance through the elimination of self-reactive clones[6]. Notably, many PASLI/APDS patients are positive for autoantibodies and develop autoimmune manifestations, such as glomerulonephritis[16]. Similarly, we found increased IgG and IgM anti-nuclear antibodies (ANA) in sera of mutant mice (Fig. 6a and Supplementary Fig. 6a). Evaluation using an array of 94 different auto-antigens revealed that IgM and IgG antibodies directed against approximately 50 auto-antigens were significantly increased in mutant compared to wild-

type mice (Fig. 6b, Supplementary Fig. 6b and Supplementary Table 2). Moreover, 1-year-old mutant mice exhibited lymphocytic infiltration in multiple organs (Fig. 6c). Thus, *Pik3cd*$^{E1020K/+}$ mice exhibited increased self-reactive antibodies and tissue lymphocytic infiltration that worsened with age.

Increased gut-associated GCs with higher IgA-coated fecal bacteria

It is now appreciated that there are numerous connections between the commensal microbiome and autoimmunity[29]. To evaluate whether microbiota contributed to activated phenotypes in *Pik3cd*$^{E1020K/+}$ mice, we examined mesenteric lymph nodes (mLN) and Peyer's patches (PPs), which are continuously exposed to a wide range of microbiota and food-derived antigens that sustain T_{FH} and GC B cell generation[30]. Again, we found increased cellularity, as well as higher numbers of T_{FH} and GC B cells in mutant mLN and PPs (Fig. 7a,b). Furthermore, whereas wild-type mLNs contained GCs predominantly in the cortical region, mutants displayed increased GCs scattered throughout the internal medullary area (Supplementary Fig. 7a,b). Mutant mLNs also displayed disorganization of GC with poor demarcation of DZ and LZ areas, and PD-1^{+} T_{FH} cells infiltrating the DZ (Supplementary Fig. 7a,c,d), as in peripheral LNs.

T_{FH} cells play a crucial role in supporting the selection of GC B cells, and differentiation to IgA-secreting plasma cells in response to commensal stimulation in gut[31]. Accordingly, higher free fecal IgA as well as fecal IgA-coated bacteria were detected in *Pik3cd*$^{E1020K/+}$ mice (Fig. 7c,d). To identify gut bacterial taxa preferentially targeted by IgA, we sorted IgA-coated and uncoated bacteria and performed 16S rRNA sequencing for wild-type and *Pik3cd*$^{E1020K/+}$ mice. Multiple bacterial taxa exhibited greater IgA coating in *Pik3cd*$^{E1020K/+}$ mice compared to wild-type. Although these did not reach statistical significance after correction for multiple testing, these taxa outnumbered those less targeted by IgA in *Pik3cd*$^{E1020K/+}$ versus wild-type mice (Fig. 7e and Supplementary Table 3). Intriguingly, these included *Akkermansia muciniphila*, a commensal bacterium that is highly abundant in the human gut[32] (Fig. 7f). The overall community structure of the microbiota did not differ consistently between wild-type and mutants (Supplementary Fig. 7e,f). However, phylogenetic diversity, which reflects the richness in number and phylogenetic distribution of taxa within a single community, was significantly lower in mutant mice, and was inversely correlated with the percentage of IgA-coated bacteria (Fig. 7g,h), similar to mouse models with strong mucosal IgA responses[33].

Heightened systemic responses to gut bacteria

Given potential connections between autoreactive and anti-commensal antibodies[29], we examined the serum for anti-commensal IgG. We detected significant increases in serum IgG2a/b that bound fecal bacteria in mutant mice (Fig. 8a), indicative of higher systemic responses to gut commensals. Moreover, we found elevated IgG binding to *A. muciniphila*, but not to a control bacterium, *Lactobacillus reuteri*, (Fig. 8b), supporting specificity of these responses.

Furthermore, splenic follicular B cells showed increased responsiveness and lower thresholds for expression of activation markers in response to autologous fecal microbiome

extracts (Fig. 8c), as well as LPS, an innate TLR agonist released by gut bacteria (Fig. 8d). Thus, *Pik3cd*$^{E1020K/+}$ increased both antigen-specific and innate reactivity towards commensal-derived products.

Antibiotics reduce activated-phenotypes and autoantibodies

To evaluate potential connections between anti-commensal responses and autoimmunity, we examined the antibodies that specifically bound fecal bacteria. Mutant serum antibodies that bound gut bacteria and were subsequently eluted, showed increased binding of dsDNA, suggesting possible cross-reactivity with self-antigens (Fig. 8e).

To determine whether gut commensals directly contributed to immune activation in *Pik3cd*$^{E1020K/+}$ mice, we treated wild-type and mutant littermates with a cocktail of antibiotics for 6 weeks, starting at weaning. Antibiotic treatment reduced splenic cellularity, as well as numbers of activated CD4$^+$ T cells, T_{FH} cells and percentages and numbers plasma cells in the spleens of mutant, but not wild-type mice (Fig. 8f-i). Notably, antibiotic treatment reduced total IgG, as well as antibodies directed against dsDNA and multiple self-antigens, to levels seen in wild-type mice (Fig. 8j-l). Thus, the generation of hyperactivated and autoreactive phenotypes in *Pik3cd*$^{E1020K/+}$ mice requires signals derived from commensal stimuli.

DISCUSSION

Using a mouse model that recapitulates features of PASLI/APDS, we found increased T_{FH} and GC B cells, yet inefficient class-switched antigen-specific B-cell responses to immunization. Nonetheless, *Pik3cd*$^{E1020K/+}$ mice exhibited increased antibodies toward commensal bacteria and self-antigens, the latter of which were strikingly reduced by antibiotic treatment. Our data suggest that PI3Kδ selectively controls lymphocyte activation, allowing efficient generation of protective responses, while preventing excessive reactivity to tonic stimulation by commensals that can promote lymphoid dysregulation.

Several factors may contribute to aberrant humoral immunity in *Pik3cd*$^{E1020K/+}$ mice. T_{FH} cells, normally confined to the LZ, specifically target high-affinity B cells, inducing survival and proliferation. In contrast, increased T_{FH} cell numbers may decrease competition for survival signals provided to B cells and paradoxically impair specific responses[22]. Furthermore, T_{FH} cells abnormally located in the DZ in mutant GCs may drive inappropriate signals[34], including PI3K-mediated pathways in B cells. Of note, PASLI/APDS patients also show disrupted GC architecture with increased T_{FH} cell invasion[16]. This mislocalization of T_{FH} cells is intriguing, given that PI3K pathways regulate multiple molecules involved in lymphocyte migration[1]. Our analyses also revealed increased Foxp3$^+$ T_{reg} and T_{FR} cells in mutant mice. However, while increased T_{FR}:T_{FH} ratios can impair humoral responses[35], we observed ratios comparable to wild-type. Finally, increased GC and T_{FH} cells, which completely fill the FDC networks over time, likely contribute to impaired development of new antigen-specific responses, particularly with age.

Like FOXO1-deficient T cells[11], mutant CD4$^+$ T cells exhibited ICOS-independent T_{FH} cell differentiation. However, despite previous data arguing for a more important role for PI3Kδ

in T_{FH} cells than in GC B cells[15], we found that *Pik3cd*$^{E1020K/+}$ B cells intrinsically generate more GC B and plasma cells, with increased p-FOXO1. Mirroring the requirements for FOXO1 in DZ formation, AID regulation and generation of antigen-specific responses[36,37], *Pik3cd*$^{E1020K/+}$ mice also have defective IgG1 switching and lower DZ/LZ ratios. Thus, mutant mice recapitulate phenotypes of FOXO1-deficient T and B cells, although less severe.

Previous data using an activated ubiquitously expressed p110α isoform support its role in tonic BCR signaling required for B cell survival[27]. Similarly, we found increased survival of PI3Kδ$^{E1020K/+}$ activated B cells, associated with altered expression of BIM and MCL-1. Interestingly, BIM-deficient mice succumb to SLE-like autoimmunity with an accumulation of self-reactive lymphocytes and autoantibodies[38]. MCL1 is critical for memory B and plasma cell formation[39,40]. Together, these factors may impair the selective pruning required for proper antigen-specific responses.

Pik3cd$^{E1020K/+}$ mice exhibit higher GALT-associated lymphoid-activation and percentages of both fecal IgA- and serum IgG-binding fecal bacteria. IgA-coated bacteria are enriched in commensal pathobionts that can drive intestinal and systemic inflammation in particular disease settings[41]. Notably, we detected GCs in the medullary region of mutant mLN, which is normally only observed with inflammation[42]. Among bacterial species preferentially bound by IgA in mutant mice we found *A. muciniphila*, which promotes IgA responses[32,41] and is associated with protective effects in diabetic models[43] and cancer immunotherapy[44]. We speculate that alterations in the prevalence of highly IgA-coated bacteria may amplify auto-reactive responses under certain genetic conditions, such as in *Pik3cd*$^{E1020K/+}$ mice.

Our data support a strong connection between the microbiota and autoimmunity in PASLI/APDS. Systemic responses toward gut bacteria could neutralize commensals that spread systemically when gut barriers are leaky[45,46], as proposed for MYD88- and IRAK-4-deficient patients, who have increased B cells expressing VH4–34, which cross-reacts with self-antigens and commensals[47]. However, immune responses towards microbiota may also amplify auto-reactive lymphocytes, causing immune pathology in peripheral sites, as reported for other autoimmune conditions[29]. While altered gut-integrity may contribute to increased anti-commensal reactivity, mucosal barriers appeared grossly intact in mutant mice. We therefore speculate that activated PI3Kδ lowers the threshold for signaling from receptors on T and B cells, making them more susceptible to activation by commensal products physiologically released in the periphery. Although we found IgG reactive to *A. muciniphila* but not to a control *Lactobaccillus* nor to *phosphorylcholine (PC)*, which is used to identify poly-reactive antibodies (data not shown), we cannot rule out a general relaxation of tolerance and non-antigen specific activation by gut bacteria. However, the elevated commensal antigen-specific IgG in conjunction with increased responsiveness of mutant B cells to autologous fecal material and LPS, suggest that activated PI3Kδ drives hyperesponsiveness to both antigens and innate stimuli. In contrast, these commensal stimuli may be suboptimal to trigger downstream pathways in wild-type cells with tightly tuned PI3Kδ activity.

Our findings underscore the importance of PI3Kδ in the activation of T and B cells required for proper GC reactions, where both too little[15] and too much PI3Kδ activity disrupt humoral immunity. Importantly, we have uncovered an unappreciated role for PI3Kδ in modulating responses to the commensal microbiota, that, if not properly controlled, can lead to lymphoid hypereactivity that worsens with age. Recent work has shown promising results with PASLI/APDS patients treated with a PI3Kδ inhibitor[48]; however the long-term consequences of this treatment remain unknown, especially given data demonstrating associated genomic-instability[49]. Our work may provide new perspectives on managing patients with activated PI3Kδ, as well as other autoimmune conditions, including those induced by checkpoint-blockade therapy, where dampening PI3K pathways may allow the selective control of immune responses.

Methods

Patient samples.

All human subjects and their guardians in this study signed written informed consent in accordance with Helsinki principles for enrollment in research protocols that were approved by the Institutional Review Board of NIAID (clinical trial registration number NCT00001355, US NIH). Blood from healthy donors was obtained at the NIH Clinical Center under approved protocols. All procedures were based on standard of care, under established clinical guidelines. Peripheral blood mononuclear cells (PBMCs) were isolated using Ficoll-Hypaque gradient centrifugation. Blood T_{FH} cells were stained at 20°C (room temperature) using antibodies indicated in the reporting summary and figure legends.

Mice.

C57BL/6 (000664), OT- II (004194), ZP3-Cre (003651), CD45.1 (002014), BLIMP-1-YFP (008828), and MD4 (002595) mice were obtained from The Jackson Laboratory. Rosa26-HA-hFoxo1AAA (Foxo1^{AAA}) mice[26], were bred to OT-II *Pik3cd*$^{E1020K/+}$ mice. To generate *Pik3cd*$^{E1020K/+}$ mice, a targeting construct was built by mutagenizing exon 24 to introduce a G to A point mutation encoding E1020K and subcloning flanking fragments into the PL452 vector. The targeting construct was linearized with NotI and electroporated into HG-3 129/Sv × C57BL6/J ES cell line together with a TALEN that cut in the intron upstream of exon 24 to increase targeting. Genomic DNA was isolated from 48 G418-resistant ES clones and initially screened by PCR using outside primers for both targeting arms; 4 clones were confirmed positive by Southern blot analysis using DraI and ApaII and 5′ and −3′ flanking probes, respectively and by sequencing for the point mutation. Cells were microinjected into blastocytes from C57BL6/J mice and progeny positive for the targeted allele were crossed to ZP3-Cre mice to delete the *neo*^{r} gene in the female germline. Positive mice were backcrossed to C57BL6/J mice, SNP genotyped (Dartmouse) to obtain mice that were >99.6% C57BL6/J, and maintained heterozygous for the mutant allele. For adoptive transfer experiments, *Pik3cd*$^{E1020K/+}$ mice were bred to OT-II or MD4 mice positive for the CD45.1, CD45.2 or CD45.1/2 alleles. Mice were maintained and treated under specific pathogen-free (SPF) conditions in accordance with the guidelines of the NHGRI Animal Care and Use Committee at the NIH (protocol G98–3).

Mouse flow cytometry.

Antibodies and dilutions are described in the reporting summary. For staining, single cell preparations were made from spleen and lymph node in MACS buffer (PBS with 2% FBS and 2 μM EDTA). Staining panels containing anti-CD93 (Supplementary Fig. 1d) were performed in MACS buffer not supplemented with EDTA. After ACK (Ammonium Chloride) lysis of RBCs, cells were washed once and Fc receptors blocked with anti-mouse CD16/32 (2.4G2, BioXCell). Cells were incubated with antibodies for 45/60 min on ice. Intracellular staining of BCL-6, Foxp3 and MCL-1 were performed using the Foxp3-staining buffer set from eBioscience. The following reagents were used according to the manufacture instructions: PhiPhiLux-G1D2 kit (OncoImmunin Inc.), Annexin V-FITC (BD Biosciences) and Annexin V binding buffer (BioLegend), CellTrace™ Violet (CTV) Cell Proliferation Kit from Life Technologies, LIVE/DEAD® Fixable Aqua Dead Cell Stain Kit and LIVE/DEAD® Fixable Near-IR Dead Cell Stain Kit (Life Technologies). The following gates were applied before the identification of the specific cell types: FSC-A/SSC-A, exclusion of doublets (SSC-H/SSC-W and FSC-H/FSC-W), live cells (negative for Aqua or Near-IR dead stain kit); gating strategies for each population are indicated in each figure legend. Flow cytometry was performed on a LSRII (BD Biosciences) and data analyzed using FlowJo 9.9 software (TreeStar).

ELISA.

ELISA for total and antigen-specific immunoglobulin was performed as previously described[22]. Plates (Costar) were coated ON with 5 μg/ml anti-Ig antibodies or NP_{20}-BSA and NP_4-BSA (Biosearch Technologies) in PBS at 4°C. Plates were blocked with 1% BSA/PBS, serial dilutions of sera were applied and incubated at 20°C (room temperature) for 2–3 h. Subsequently, plates were washed (with PBS/0.05% Tween20) and incubated with alkaline phosphatase (AP)-conjugated anti-mouse Ig isotype-specific antibodies followed by pNPP substrate (Sigma-Aldrich) as detection reagents. Absorbance was measured at 405_{nm} with a microplate reader (Molecular Devices) and values were calculated according to Ig standards or to reference serum from wild-type mice immunized twice with NP_{19}-OVA (expressed in arbitrary units, AU). Ratios between NP_{4-} versus NP_{20}-binding antibodies were calculated as an estimate for affinity maturation. Fecal IgA ELISA were performed as previously described[50]: fresh stools were collected, dissolved in PBS (100 μl/0.01 g), centrifuged, and IgA concentrations determined by ELISA on the recovered supernatants. Antibodies and immunoglobulin standards were purchased through Southern Biotech.

Histology.

Mouse organs were fixed ON at 20°C (room temperature) in Neutral Buffered Formalin. After fixation, samples were dehydrated in 70% Ethanol and embedded in paraffin, microtome cut (8–10 μm) and H&E stained (Histoserv, Inc.). Immunohistochemical images were acquired on an upright Zeiss Axio Imager D2 microscope (Carl Zeiss Inc.) with 1×, 5× or 10× objective lenses, using a AxioCam HRc full color CCD camera. Zeiss ZEN blue pro 2011 software package was used for collection and for post-processing of the images.

White blood cell counts.

Mouse blood samples were collected in K_2EDTA Microtainer tubes (BD), and blood cell counts obtained on a ADVIA® 2120/2120i Hematology System (NIH, Clinical Center).

Adoptive cell transfers.

Wild-type and *Pik3cd*$^{E1020K/+}$ naive OT-II cells were enriched using a T cell negative-selection kit (Miltenyi Biotec), then CD4$^+$CD8$^-$CD44^{lo}CD62L$^+$CD25$^-$cells sorted on a FACSAria cell sorter (BD Biosciences) to >95% purity. Anti-CD43 antibody-conjugated microbeads (Ly-48) (Miltenyi Biotec) were used to isolate naïve wild-type and *Pik3cd*$^{E1020K/+}$ B cells. Naïve OT-II cells (1–2 × 10^5 per mouse), MD4 HEL-specific B cells (1–2 × 10^5 per mouse) or polyclonal B cells (5–6 × 10^6 per mouse) were injected intravenously (i.v.) and allowed to equilibrate within the host for 16–24 h before immunization. For expression of Foxo1^{AAA}, CAG-GFP-IRES-CRE (Plasmid #48201, Addgene) and pCL-Eco (Addgene) were transfected into 293 T cells (ATCC) with TransIT-293® Transfection Reagent (Mirus). Supernatants were collected after 24 and 48 h. Naïve wild-type or *Pik3cd*$^{E1020K/+}$ OT-II and wild-type or *Pik3cd*$^{E1020K/+}$ HA-hFoxo1^{AAA} OT-II cells were activated *in vitro* with 5 μg/ml of platebound anti-CD3 (2C11; BioXCell) and 5 μg/ml of anti-CD28 (37.51; BioXCell). Twenty-four and 40–44 h post activation, CRE-GFP retroviral supernatants were added to T cells and spun at 2500 rpm for 1.5 h at 30–35 °C with 8 μg/ml polybrene (Sigma) and rhIL-2 (10 U/ml). On day+3, GFP$^+$ cells were FACS sorted and i.v. injected into wild-type hosts that were immunized i.p. with NP-OVA 48 h later, and analyzed on day+5 in the spleen. Cells were stained intracellularly with anti-HA (6E2, Cell Signaling Technology) to detect Foxo1^{AAA} expression within the GFP$^+$ cells.

Antigens and immunizations.

For OT-II transfer experiments, mice were immunized intraperitoneally (i.p.) with 50 μg of NP-OVA (Biosearch Technologies) in alum (Imject™ Alum Adjuvant, Thermo Scientific). For MD4 and OT-II cell co-transfers, mice were immunized i.p. with 25 μg of HEL^{WT}-OVA$_{323–339}$ in alum (kindly provided by Humabs BioMed, Bellinzona, Switzerland). For subcutaneous immunization, mice received 20 μg of NP-OVA in alum in the hock. Analyses were performed 7–8 days post-immunization.

In vivo anti-ICOS-L blocking.

For OT-II transfer experiments, 100 μg of anti-ICOS-L (HK5.3) or isotype control (BioXCell) were given i.v. on day-1, then i.p. every other day until the day of sacrifice. For treatment of wild-type and *Pik3cd*$^{E1020K/+}$ mice, antibodies were given i.v. on day 0 and i.p. on day +2, +4, +6.

In vitro experiments.

For *in vitro* B cell proliferation, live naïve follicular (FO) B cells were isolated with anti-CD43 antibody-conjugated microbeads, then sorted as B220$^+$CD19$^+$CD23$^+$CD21$^+$GL-7$^-$FAS$^-$CD138$^-$Aqua/live/dead$^-$ on a FACSAria (BD), stained with CTV and cultured with different stimuli: 5 μg/ml F(ab')$_2$ goat anti-mouse IgM

(Jackson ImmunoResearch), 10 μg/ml rat anti-mouse CD40 (BD Bioscience), 1 μg/ml LPS from *E. coli* (Enzo Life Sciences), 2 ng/ml recombinant murine IL-4 (Peprotech), 200 ng/ml human BAFF (R&D), or 10 ng/ml recombinant murine IL-21 (Peprotech), 5 ng/ml HEL (Sigma). After 3–4 days, B cells were assessed for activation, differentiation and cell division by flow cytometry. In certain experiments, B cells were treated with 3.7 pM CAL-101 (Santa Cruz Biotechnology), a selective PI3Kδ inhibitor for 3 days. For *in vitro* analysis of BrdU incorporation by B cells, cells were treated with 10 μM BrdU for 45 min on day+2 post stimulation with anti-IgM, then stained with FITC BrdU Flow Kit (BD Biosciences), as per manufacturer. For p-FOXO1 staining, B cells were first rested for 1 h at 37 °C in serum-free RPMI. p-AKT and p-S6 staining were performed on naïve T and B cells isolated using naïve $CD4^+$ T cell isolation kit and anti-CD43 antibody-conjugated microbeads (Miltenyi Biotec). In some cultures, T and B cells were pre-treated with 2 nM CAL-101, or vehicle, for 1 h and then stimulated with platebound 2 μg/ml anti-CD3 and 5 μg/ml anti-CD28, or anti-IgM (5 μg/ml), for different times. For *in vitro* p-FOXO1 detection, sorted naïve polyclonal wild-type or *Pik3cd*$^{E1020K/+}$ T cells were stimulated *in vitro* with 5 μg/ml of anti-CD3 (platebound) and anti-CD28. After 3–4 days, activated T cells were washed, rested for 2 h at 37 °C in serum-free RPMI, then stimulated for 1 h with 5 μg/ml of anti-ICOS (C398.4A; BioLegend) cross-linked with 5 μg/ml of anti-Hamster IgG (Jackson ImmunoResearch). For intracellular staining of phosphoproteins, cells were fixed with 4% PFA, permeabilized with cold methanol at –20°C ON as previously described[51], and stained with p-AKT S437, p-S6 Ribosomal Protein (Ser240/244), p-S6 Ribosomal Protein (Ser235/236), and polyclonal phospho-FOXO1(Ser256) followed by AF488 goat anti-rabbit IgG (Invitrogen); antibody information is provided in the reporting summary. *In vitro* stimulation of OT-II cells with 0.6–2 ng/ml $OVA_{323–339}$ (# 27025; AnaSpec Inc.) was performed with $CD11c^+$ DCs from wild-type mice (isolated using Miltenyi Biotec CD11c microbeads) for 20 h (T:DC ratio 1:1). Intracellular staining for IL-21 was performed on FACS sorted wild-type or mutant OT-II non-T_{FH} cells ($PD\text{-}1^-CXCR5^-$) and T_{FH} cells ($PD\text{-}1^+$ $CXCR5^+$) isolated after transfer into wild-type mice 7 days post immunization. OT-II cells were re-stimulated *in vitro* for 4 h with PMA (Sigma, 20 ng/ml), ionomycin (1 μg/ml, Sigma) and golgi stop (1:1000, BD Biosciences) and stained for IL-21 using recombinant mouse IL-21R-Fc Chimera (R&D) followed by secondary R- Phyco affinity pure R(ab')2 fragment goat anti-human IgG, Fcγ Frag Spec (Jackson ImmunoResearch). *In vitro* T–B cell co-cultures (T:B ratio 1:1) were performed using wild-type B cells ($CD43^-$), isolated from naïve wild-type spleen, together with polyclonal wild-type or mutant FACS sorted T_{FH} cells ($CD4^+CD25^-PD\text{-}1^+CXCR5^+$), isolated on day+7 from the spleen of i.p. NP-OVA immunized mice, and re-stimulated with anti-IgM (5 μg/ml) and anti-CD3 (1 μg/ml) for 7 days. Microbiome extract was prepared from stool samples isolated from the large intestine of wild-type and mutant mice as previously described[52]. cOmplete™ Mini Protease Inhibitor Cocktail (Roche) together and 0.5 mM phenylmethylsulfonyl fluoride (Sigma) were used to prepare the protease inhibitor cocktail to resuspend the bacterial pellet. Protein extract concentration was calculated through Pierce™ BCA Protein Assay Kit. FACS sorted naïve splenic wild-type or mutant follicular (FO) B cells were stimulated *in vitro* with serial dilutions of the extract for 20 h and treated with or without 1 nM CAL-101.

Immunohistochemistry and confocal microscopy.

Immunohistochemistry was performed as previously described[53]. Organs were harvested and fixed for 24 h with BD CytoFix/CytoPerm (BD Biosciences) diluted in PBS (1:4), washed in PBS and incubated in 30% sucrose ON before embedding in OCT compound (Tissue-Tek). 30 μm sections were cut on a CM3050S cryostat (Leica) and adhered to Super Frost Plus Gold slides (Electron Microscopy Services). Frozen sections were permeabilized and blocked for 1–2 h in PBS containing 0.3% Triton X-100, 1% BSA, and 1% Fc block. Sections were stained with directly conjugated antibodies for 12 h at 4 °C in a humidity chamber in the dark. Antibody information provided in the reporting summary. Cell nuclei were visualized with JOJO-1 (Thermo Fisher Scientific). Stained slides were mounted with Fluoromount G (eBioscience) and sealed with a glass coverslip. Large tile scans spanning the entire LN were acquired using a SP8 confocal microscope (Leica) equipped with a 40× objective (NA 1.3), 2 HyD and 3 PMT detectors, and 6 lasers (UV, Argon, DPSS 561, OHeNe, HeNe, 690 Diode) capable of 9 excitation wavelengths (405, 458, 476, 488, 514, 561, 594, 633, 690 nm). All images were captured at an 8-bit depth, with a line average of 3, and 1024×1024 format with the following pixel dimensions: x (0.284–0.378 μm), y (0.284–0.378 μm), and z (1–1.25 μm).

Histocytometry.

Histocytometry analysis was performed as previously described[54]. An 8-color panel was developed consisting of the following fluorophores: Brilliant Violet 421, Brilliant Violet 510, Alexa Fluor 488, JOJO-1, PE, Alexa Fluor 594, Alexa Fluor 647, and Alexa Fluor 700. Fluorophore emission was collected on separate detectors with sequential laser excitation used to minimize spectral spillover. The Channel Dye Separation module within the LAS AF software (Leica) was then used to correct for any residual spillover. Representative tile scans were taken at a voxel density of 1024×1024 and 1 μm z step. Threshold identification, voxel gating, surface creation, and masking were performed as previously described[55]. For publication quality images, Gaussian filters, brightness/contrast adjustments, and channel masks were applied uniformly to all images. Images are presented as maximum intensity projections (MIP) of tiled z-stacks. Histo-cytometric quantification of cell surfaces was based on images with unadjusted gamma values. Cells were segmented on PD-1$^+$, CD4$^+$, CD35$^+$, or BCL-6$^+$ surfaces to create T_{FH} cells, FDC networks, and GCs, respectively. Channel statistics for all surfaces were exported into Excel (Microsoft) and converted to a csv file for direct visualization in FlowJo v10.1r5 (Treestar). GC gates were defined using positional data on the BCL-6$^+$ surfaces. LZ and DZ gates were drawn using the density of CD35$^+$ and BCL-6$^+$ surfaces within the GC. These positional gates were then applied to PD-1$^+$CD4$^+$ surfaces to calculate the percentage of T_{FH} cells in the DZ for each GC. To normalize the numbers of T_{FH} cells per GC areas, T_{FH} cell surfaces were first created in Imaris using PD-1 and CD4 expression levels. The “analyze particle” function in Fiji was used to quantify the numbers of T_{FH} cells per DZ (CD35^{lo} and BCL-6^{hi}). These numbers were then divided by the area of each region (also obtained by Fiji) and normalized to an arbitrary area.

Autoantibodies.

Anti-dsDNA and anti-ANA IgG or IgM were determined using kits from Alpha Diagnostic according to the manufacturer. Screening for a panel of IgG and IgM autoantibodies was performed with autoantibody arrays (University of Texas Southwestern Medical Center, Genomic and Microarray Core Facility) as described[56]. Diluted serum samples from wild-type, *Pik3cd*$^{E1020K/+}$ and MRL/NZM mice were incubated in duplicate with the autoantigen arrays and binding was detected with fluorescent anti-Ig antibodies (IgG and IgM). TIFF images were analyzed using Genepix Pro 6.0 softwares. Net fluorescence intensity data (defined as the spot minus background fluorescence intensity) from duplicate spots were averaged. Signal-to-noise ratios equal or greater than 3 were considered true signals. Data were normalized as follow: immunoglobulin positive control (IgG or IgM) across all samples were averaged and positive controls in each sample were divided by the averaged positive control generating a Normalization Factor (NF) for each sample. Each signal was then multiplied by the NF. Values from control samples for each antigen were averaged and ratios were calculated between each sample and the average of negative controls plus 2 standard deviations. A heat map of the ratio values was generated using Multi experiment viewer software (MeV, DFCI Boston, MA) and values were coded as follow: 0 blue, 1 black, 3 yellow, as indicated. Significant differences were determined using the significance analysis of microarray (SAM, Stanford University Labs) with a false discovery rate=0.

Mixed bone marrow chimera generation.

Host wild-type mice heterozygous CD45.1/2^{+} were sub-lethally irradiated with a single dose of 900 rad using a cesium source. Several hours later, mice were transplanted with different mixtures of wild-type (CD45.1^{+}) or *Pik3cd*$^{E1020K/+}$ (CD45.2^{+}) bone marrow cells (5×10^6 total cells, ratios 20:80, 80–20, 50:50 ratio). Mice were maintained on acid water for 5–6 weeks and analyzed after 8–12 weeks.

Fecal IgA- and serum IgG-binding bacteria.

Stool or fecal content from colons were isolated and dissolved in staining buffer, SB, (1%BSA/PBS), then spun at 500 *g* to pellet larger particles. The supernatant was then spun at high speed, the pelleted material washed once, re-suspended in SB and combined with Syto-62 (Red Fluorescent Nucleic Acid Stain, Thermo Fisher Scientific) to detect bacterial DNA and stained with anti-IgA (11-44-2; eBioscience) or isotype control in 96-well V-bottom plates. For detection of serum IgG coated bacteria, serum was first heat-inactivated at 56 °C for 30 min. Bacteria were washed twice in SB and resuspended at 10^6 cfu per staining condition. Bacterial pellets were incubated in heat-killed serum diluted to 1:50, washed, and subsequently stained, alone or in combination, with anti-IgG1 (A85–1; BD Bioscience), anti-IgG2$_{a+b}$ (X57; BD Bioscience), which cross-reacts with IgG2$_{c+b}$ in C57BL/6 mice, anti-IgG3 (110009S; Southern Biotech), and Syto-62. Percentage of IgG-coated bacteria and mean fluorescence intensity were calculated of all Syto-62 positive events. For stripping of serum IgG from commensals, fecal bacteria (previously incubated with serum as described above) were pelleted and washed 4 times with SB to remove the unbound fraction; bound antibodies were stripped from the pellet using 0.1 M glycine pH 2.9, incubated for 30 sec and spun for 2 min at maximum speed in a microcentrifuge.

Supernatant containing IgG was recovered, put in 1/10 volume of Tris pH 8, and tested for binding to dsDNA by ELISA.

Gut microbiota sequencing.

Wild-type and *Pik3cd*$^{E1020/+}$ littermates were separated at weaning and placed in different cages based on their genotype. Unfractionated bacterial pellets, prepared as described in the previous section, were stored at –80 °C until use. In parallel, IgA-coated fecal bacteria stained with anti-IgA-PE were followed by anti-PE antibody-conjugated microbeads (Miltenyi Biotec). IgA negative and positive bacteria were enriched through positive selection by running through MACS columns (Miltenyi Biotec) twice. Enriched bacteria were centrifuged and pellets were stored at –80 °C until use. Bacterial genomic DNA was purified using phenol:chloroform extraction followed by ethanol precipitation and purification using the QIAquick PCR Purification Kit (Qiagen). Amplification of the V4 hypervariable region of the bacterial 16S rRNA gene was performed using the 515f and 806r primers (515F: 5′-GTGCCAGCMGCCGCGGTAA; 806R: 5′-GGACTACHVGGGTWTCTAAT), followed by an additional PCR to append unique barcodes to each sample. Amplicons were quantified using Qubit (Thermo Fisher Scientific) and pooled at equimolar concentrations before being sequenced on an Illumina MiSeq instrument using the V2 MiSeq Reagent kit (Illumina). The dada2 algorithm[57] was used to denoise 16S reads after primer trimming and to tabulate sequence variants. Rarefaction was performed to 70,000 reads per sample. IgA scores were calculated for each taxon within each murine sample pair (IgA+, IgA–) by log-transforming all taxon abundances and subtracting IgA-uncoated fraction abundances from the IgA-coated fraction abundances. Taxa that were not detected in either the IgA+ or IgA– fraction for a given mouse were excluded from statistical analyses on a per-mouse basis.

In vivo antibiotic treatment.

Wild-type and *Pik3cd*$^{E1020/+}$ littermates were separated at weaning and placed in different cages based on their genotype. Right after weaning, mice were treated for 5–6 weeks with a mixture of ampicillin (1 g/l), metronidazole (1 g/l), neomycin (1g/l), vancomycin (0.5 g/l), in drinking water. No calorie sweetener (6 gr/l) was added to the antibiotic. Control groups received sweetener alone.

Semi quantitative real time PCR.

FACS sorted wild-type or *Pik3cd*$^{E1020K/+}$ splenic GC B cells were directly lysed in TRIzol LS reagent (Invitrogen). RNA was isolated using a Qiagen microRNA isolation kit, and transcribed into cDNA. Taqman probes were used with TaqMan® Universal PCR Master Mix (Thermo Scientific) according to the manufacturer's instructions to amplify *Bcl2l11* (Mm00437796_m1) mRNA. 18S (4319413e, Thermo Scientific) was used to normalize and calculate relative expression.

Statistical analysis.

Data were analyzed via Prism 6 (GraphPad Software) or custom R scripts and the 'Hmisc' package, using parametric t tests and the non-parametric unpaired Mann-Whitney U test for

comparison of two unpaired groups. Graphs show the mean ± SEM. *$P < 0.05$; ** $P < 0.01$; *** $P < 0.001$. If not indicated, the P values were not significant (>0.05). PERMANOVA was performed using the 'adonis' function in the R package 'vegan'.

Data availability statement.—The materials, data, and any associated protocols that support the findings of this study are available from the corresponding authors upon request. Accession codes for microbiome sequences are publically available at: (https://www.ncbi.nlm.nih.gov/Traces/study/?acc=SRP132959).

Computer code availability.—The custom IgA-seq analysis R scripts that support the findings of this study are available from Ivan Vujkovic-Cvijin (ivc@nih.gov) upon request.

Reporting Summary.—Further information on experimental design is available in the Nature Research Reporting Summary.

Supplementary Material

Refer to Web version on PubMed Central for supplementary material.

Acknowledgements

We would like to thank S. Kapnick for insightful discussions and protocol suggestions; K. Mao for help with gut Swiss roll preparation; S. Wincovitch for help with bright-field microscopy; S. Anderson and M. Kirby for cell sorting; L. Perez for sharing protocols; M. Yan for help with auto-antibody arrays; F. Sallusto (IRB, Bellinzona, CH) for sharing reagents, and S. Crotty for helpful discussions. This work was supported in part by funds from the intramural programs of the National Human Genome Research Institute and National Institute of Allergy and Infectious Diseases, NIH, and RO1 AI102888–01A1 to M.O.L.

References

1. Okkenhaug K & Vanhaesebroeck B PI3K in lymphocyte development, differentiation and activation. Nat Rev Immunol 3, 317–330 (2003). [PubMed: 12669022]
2. Angulo I et al. Phosphoinositide 3-kinase delta gene mutation predisposes to respiratory infection and airway damage. Science 342, 866–871 (2013). [PubMed: 24136356]
3. Crank MC et al. Mutations in PIK3CD can cause hyper IgM syndrome (HIGM) associated with increased cancer susceptibility. J Clin Immunol 34, 272–276 (2014). [PubMed: 24610295]
4. Lucas CL et al. Dominant-activating germline mutations in the gene encoding the PI(3)K catalytic subunit p110delta result in T cell senescence and human immunodeficiency. Nat Immunol 15, 88–97 (2014). [PubMed: 24165795]
5. Mesin L, Ersching J & Victora GD Germinal Center B Cell Dynamics. Immunity 45, 471–482 (2016). [PubMed: 27653600]
6. Peperzak V, Vikstrom IB & Tarlinton DM Through a glass less darkly: apoptosis and the germinal center response to antigen. Immunol Rev 247, 93–106 (2012). [PubMed: 22500834]
7. Pratama A & Vinuesa CG Control of TFH cell numbers: why and how? Immunol Cell Biol 92, 40–48 (2014). [PubMed: 24189162]
8. Baumjohann D et al. Persistent antigen and germinal center B cells sustain T follicular helper cell responses and phenotype. Immunity 38, 596–605 (2013). [PubMed: 23499493]
9. Ueno H T follicular helper cells in human autoimmunity. Curr Opin Immunol 43, 24–31 (2016). [PubMed: 27588918]
10. Qi H T follicular helper cells in space-time. Nat Rev Immunol 16, 612–625 (2016). [PubMed: 27573485]

11. Stone EL et al. ICOS coreceptor signaling inactivates the transcription factor FOXO1 to promote Tfh cell differentiation. Immunity 42, 239–251 (2015). [PubMed: 25692700]
12. Zeng H et al. mTORC1 and mTORC2 Kinase Signaling and Glucose Metabolism Drive Follicular Helper T Cell Differentiation. Immunity 45, 540–554 (2016). [PubMed: 27637146]
13. Okkenhaug K & Burger JA PI3K Signaling in Normal B Cells and Chronic Lymphocytic Leukemia (CLL). Curr Top Microbiol Immunol 393, 123–142 (2016). [PubMed: 26350103]
14. Okkenhaug K et al. Impaired B and T cell antigen receptor signaling in p110delta PI 3-kinase mutant mice. Science 297, 1031–1034 (2002). [PubMed: 12130661]
15. Rolf J et al. Phosphoinositide 3-kinase activity in T cells regulates the magnitude of the germinal center reaction. J Immunol 185, 4042–4052 (2010). [PubMed: 20826752]
16. Coulter TI et al. Clinical spectrum and features of activated phosphoinositide 3-kinase delta syndrome: A large patient cohort study. J Allergy Clin Immunol 139, 597–606 e594 (2017). [PubMed: 27555459]
17. Schmitt N, Bentebibel SE & Ueno H Phenotype and functions of memory Tfh cells in human blood. Trends Immunol 35, 436–442 (2014). [PubMed: 24998903]
18. He J et al. Circulating precursor CCR7(lo)PD-1(hi) CXCR5(+) CD4(+) T cells indicate Tfh cell activity and promote antibody responses upon antigen reexposure. Immunity 39, 770–781 (2013). [PubMed: 24138884]
19. Dulau Florea AE et al. Abnormal B-cell maturation in the bone marrow of patients with germline mutations in PIK3CD. J Allergy Clin Immunol 139, 1032–1035 e1036 (2017). [PubMed: 27697496]
20. Chen J, Limon JJ, Blanc C, Peng SL & Fruman DA Foxo1 regulates marginal zone B-cell development. Eur J Immunol 40, 1890–1896 (2010). [PubMed: 20449867]
21. Duan B & Morel L Role of B-1a cells in autoimmunity. Autoimmun Rev 5, 403–408 (2006). [PubMed: 16890894]
22. Preite S et al. Somatic mutations and affinity maturation are impaired by excessive numbers of T follicular helper cells and restored by Treg cells or memory T cells. Eur J Immunol 45, 3010–3021 (2015). [PubMed: 26332258]
23. Victora GD et al. Germinal center dynamics revealed by multiphoton microscopy with a photoactivatable fluorescent reporter. Cell 143, 592–605 (2010). [PubMed: 21074050]
24. Sayin I et al. Spatial distribution and function of T follicular regulatory cells in human lymph nodes. J Exp Med (2018).
25. Hedrick SM, Hess Michelini R, Doedens AL, Goldrath AW & Stone EL FOXO transcription factors throughout T cell biology. Nat Rev Immunol 12, 649–661 (2012). [PubMed: 22918467]
26. Ouyang W et al. Novel Foxo1-dependent transcriptional programs control T(reg) cell function. Nature 491, 554–559 (2012). [PubMed: 23135404]
27. Srinivasan L et al. PI3 kinase signals BCR-dependent mature B cell survival. Cell 139, 573–586 (2009). [PubMed: 19879843]
28. Wensveen FM, Slinger E, van Attekum MH, Brink R & Eldering E Antigen-affinity controls pre-germinal centser B cell selection by promoting Mcl-1 induction through BAFF receptor signaling. Sci Rep 6, 35673 (2016). [PubMed: 27762293]
29. Zarate-Blades CR, Horai R & Caspi RR Regulation of Autoimmunity by the Microbiome. DNA Cell Biol 35, 455–458 (2016). [PubMed: 27463238]
30. Reboldi A & Cyster JG Peyer's patches: organizing B-cell responses at the intestinal frontier. Immunol Rev 271, 230–245 (2016). [PubMed: 27088918]
31. Macpherson AJ, Koller Y & McCoy KD The bilateral responsiveness between intestinal microbes and IgA. Trends Immunol 36, 460–470 (2015). [PubMed: 26169256]
32. Derrien M, Belzer C & de Vos WM Akkermansia muciniphila and its role in regulating host functions. Microb Pathog 106, 171–181 (2017). [PubMed: 26875998]
33. Kawamoto S et al. Foxp3(+) T cells regulate immunoglobulin a selection and facilitate diversification of bacterial species responsible for immune homeostasis. Immunity 41, 152–165 (2014). [PubMed: 25017466]

34. Ersching J et al. Germinal Center Selection and Affinity Maturation Require Dynamic Regulation of mTORC1 Kinase. Immunity 46, 1045–1058 e1046 (2017). [PubMed: 28636954]
35. Sage PT & Sharpe AH T follicular regulatory cells. Immunol Rev 271, 246–259 (2016). [PubMed: 27088919]
36. Dominguez-Sola D et al. The FOXO1 Transcription Factor Instructs the Germinal Center Dark Zone Program. Immunity 43, 1064–1074 (2015). [PubMed: 26620759]
37. Sander S et al. PI3 Kinase and FOXO1 Transcription Factor Activity Differentially Control B Cells in the Germinal Center Light and Dark Zones. Immunity 43, 1075–1086 (2015). [PubMed: 26620760]
38. Hughes P, Bouillet P & Strasser A Role of Bim and other Bcl-2 family members in autoimmune and degenerative diseases. Curr Dir Autoimmun 9, 74–94 (2006). [PubMed: 16394656]
39. Peperzak V et al. Mcl-1 is essential for the survival of plasma cells. Nat Immunol 14, 290–297 (2013). [PubMed: 23377201]
40. Vikstrom I et al. Mcl-1 is essential for germinal center formation and B cell memory. Science 330, 1095–1099 (2010). [PubMed: 20929728]
41. Palm NW et al. Immunoglobulin A coating identifies colitogenic bacteria in inflammatory bowel disease. Cell 158, 1000–1010 (2014). [PubMed: 25171403]
42. Katakai T, Hara T, Sugai M, Gonda H & Shimizu A Lymph node fibroblastic reticular cells construct the stromal reticulum via contact with lymphocytes. J Exp Med 200, 783–795 (2004). [PubMed: 15381731]
43. Cani PD & de Vos WM Next-Generation Beneficial Microbes: The Case of Akkermansia muciniphila. Front Microbiol 8, 1765 (2017). [PubMed: 29018410]
44. Routy B et al. Gut microbiome influences efficacy of PD-1-based immunotherapy against epithelial tumors. Science (2017).
45. Kirkland D et al. B cell-intrinsic MyD88 signaling prevents the lethal dissemination of commensal bacteria during colonic damage. Immunity 36, 228–238 (2012). [PubMed: 22306056]
46. Slack E et al. Innate and adaptive immunity cooperate flexibly to maintain host-microbiota mutualism. Science 325, 617–620 (2009). [PubMed: 19644121]
47. Schickel JN et al. Self-reactive VH4–34-expressing IgG B cells recognize commensal bacteria. J Exp Med 214, 1991–2003 (2017). [PubMed: 28500047]
48. Rao VK et al. Effective 'Activated PI3Kdelta Syndrome'-targeted therapy with the PI3Kdelta inhibitor leniolisib. Blood (2017).
49. Compagno M et al. Phosphatidylinositol 3-kinase delta blockade increases genomic instability in B cells. Nature 542, 489–493 (2017). [PubMed: 28199309]
50. Proietti M et al. ATP-gated ionotropic P2X7 receptor controls follicular T helper cell numbers in Peyer's patches to promote host-microbiota mutualism. Immunity 41, 789–801 (2014). [PubMed: 25464855]
51. Gomez-Rodriguez J et al. Itk-mediated integration of T cell receptor and cytokine signaling regulates the balance between Th17 and regulatory T cells. J Exp Med 211, 529–543 (2014). [PubMed: 24534190]
52. Dillenburg-Pilla P, Zarate-Blades CR, Silver PB, Horai R & Caspi RR Preparation of Protein-containing Extracts from Microbiota-rich Intestinal Contents. Bio Protoc 6 (2016).
53. Radtke AJ et al. Lymph-node resident CD8alpha+ dendritic cells capture antigens from migratory malaria sporozoites and induce CD8+ T cell responses. PLoS Pathog 11, e1004637 (2015). [PubMed: 25658939]
54. Gerner MY, Kastenmuller W, Ifrim I, Kabat J & Germain RN Histo-cytometry: a method for highly multiplex quantitative tissue imaging analysis applied to dendritic cell subset microanatomy in lymph nodes. Immunity 37, 364–376 (2012). [PubMed: 22863836]
55. Gerner MY, Torabi-Parizi P & Germain RN Strategically localized dendritic cells promote rapid T cell responses to lymph-borne particulate antigens. Immunity 42, 172–185 (2015). [PubMed: 25607462]
56. Li QZ et al. Protein array autoantibody profiles for insights into systemic lupus erythematosus and incomplete lupus syndromes. Clin Exp Immunol 147, 60–70 (2007). [PubMed: 17177964]

57. Callahan BJ et al. DADA2: High-resolution sample inference from Illumina amplicon data. Nat Methods 13, 581–583 (2016). [PubMed: 27214047]

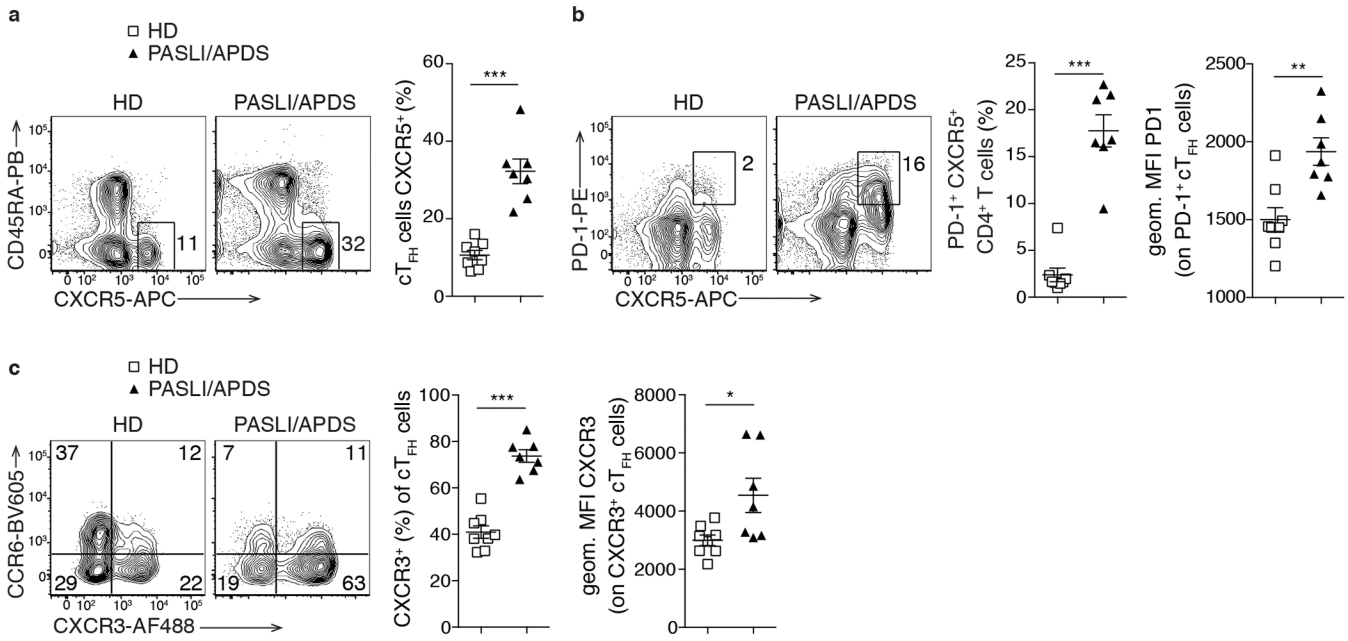

Fig. 1. Increased circulating T_{FH} cells in PASLI/APDS patients.

Analyses of blood from healthy donors (HD n=8) and PASLI/APDS patients (n=7). **a**, Representative flow plots and histogram of $CD45RA^{-}CXCR5^{+}$ cT_{FH} cells (percent of $CD4^{+}CD3^{+}CD25^{-}$ T cells). **b**, Representative contour plots and histogram of $PD\text{-}1^{+}CXCR5^{+}$ T cells (percent of $CD4^{+}CD3^{+}CD25^{-}$ T cells). Right: geometric mean fluorescent intensity (MFI) of PD-1 (gated on $PD\text{-}1^{+}$ cT_{FH} cells). **c**, Representative contour plots of $CCR6^{+}$ and $CXCR3^{+}$ cT_{FH} cells and histogram of percent of $CXCR3^{+}$ cT_{FH} (of cT_{FH} cells). Right: MFI of CXCR3 (gated on $CXCR3^{+}$ cT_{FH} cells). Data in (**a-c**) are represented as mean ± SEM with each dot indicating one individual. Significance analyzed by Mann-Whitney U test. $*P < 0.05$; $**P < 0.01$; $***P < 0.001$.

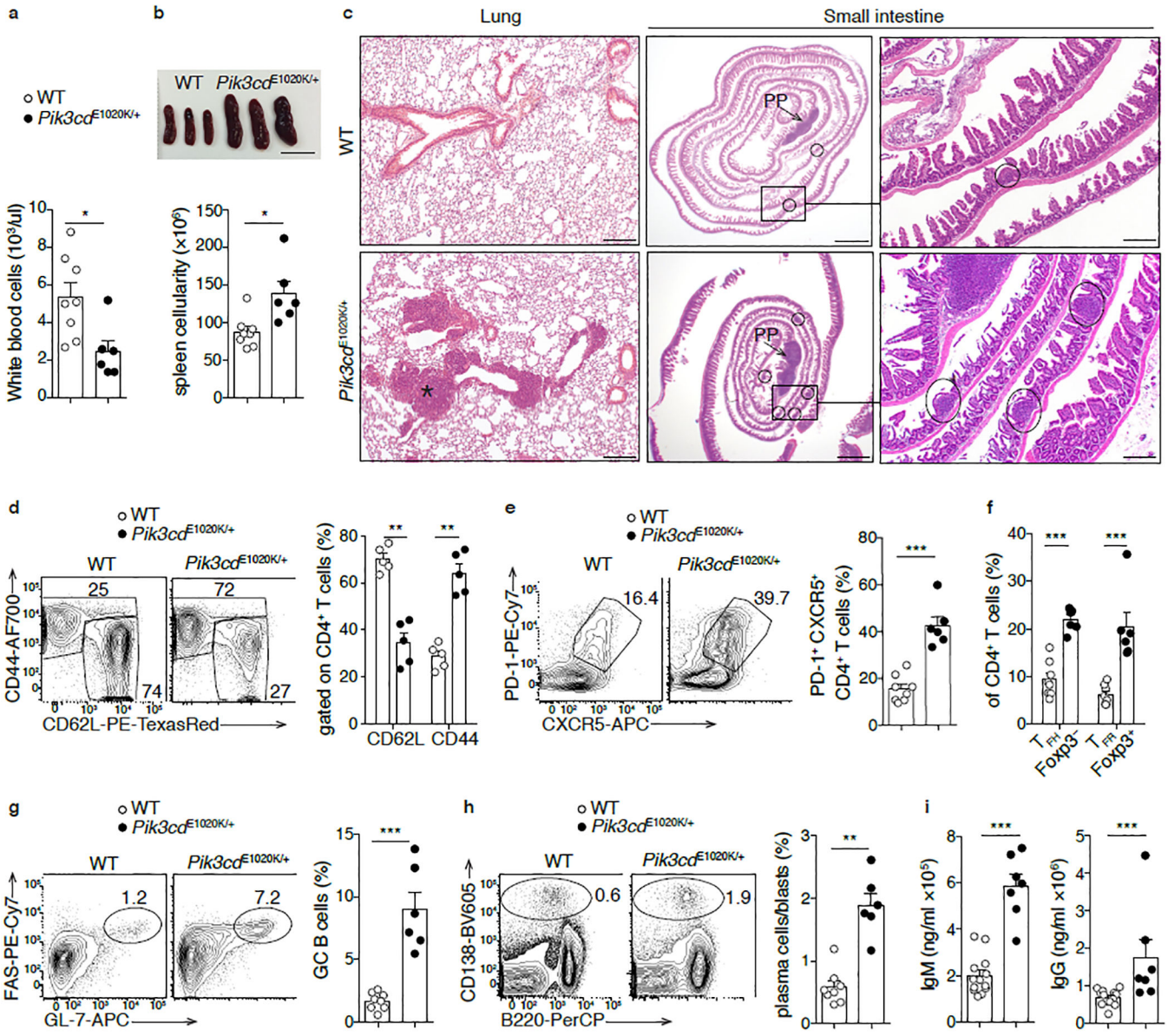

Fig. 2. *Pik3cd*$^{E1020K/+}$ mice recapitulate features of PASLI/APDS patients.

Analyses at steady state of 4-month-old wild-type and *Pik3cd*$^{E1020K/+}$ mice. **a**, White blood cell count (wild-type n=8, *Pik3cd*$^{E1020K/+}$ n=6). **b**, Spleen size (scale bar 1.27 cm) and cellularity (wild-type n=8, *Pik3cd*$^{E1020K/+}$ n=6). **c**, Left, H&E images of perfused lung sections with cell infiltration indicated with an asterisk (scale bar 200 μm). Right, small intestine Swiss roll with Peyer's patches (PPs, arrow) and isolated lymphoid follicles (ILFs, circled) (scale bar 1000 μm, and 200 μm for enlargements) (n=3 per group). **d**, Representative contour plots of splenic naïve CD44^{lo} CD62L^{+} and activated CD44^{hi} CD62L$^{—}$CD4^{+} T cells (percent of CD4^{+}B220$^{—}$ T cells) and bar graphs (n=5 per group). **e**, Representative contour plots and bar graph of PD-1^{+}CXCR5^{+}CD4^{+} T cells (percent of CD4^{+}B220$^{—}$ T cells) in the spleen. **f**, Bar graphs of Foxp3$^{—}$ T_{FH} and Foxp3^{+} T_{FR} cells among the cells gated in (**e**). **g**, Representative contour plots and histogram of FAS^{+}GL-7^{+}

GC B cells (percent of $B220^{+}CD19^{+}$ cells) in the spleen. **h**, Representative contour plots and bar graph of splenic $CD138^{+}B220^{int/lo}$ plasma cells/blasts (of live cells) (**e-h**, wild-type n=8, *Pik3cd*$^{E1020K/+}$ n=6). **i**, Total serum IgM and IgG ELISA (wild-type n=13, *Pik3cd*$^{E1020K/+}$ n=7). Data are shown as mean ± SEM with each dot indicating one mouse. Data are representative of three independent experiments. Significance analyzed by Mann-Whitney U test. $*P < 0.05$; $**P < 0.01$; $***P < 0.001$.

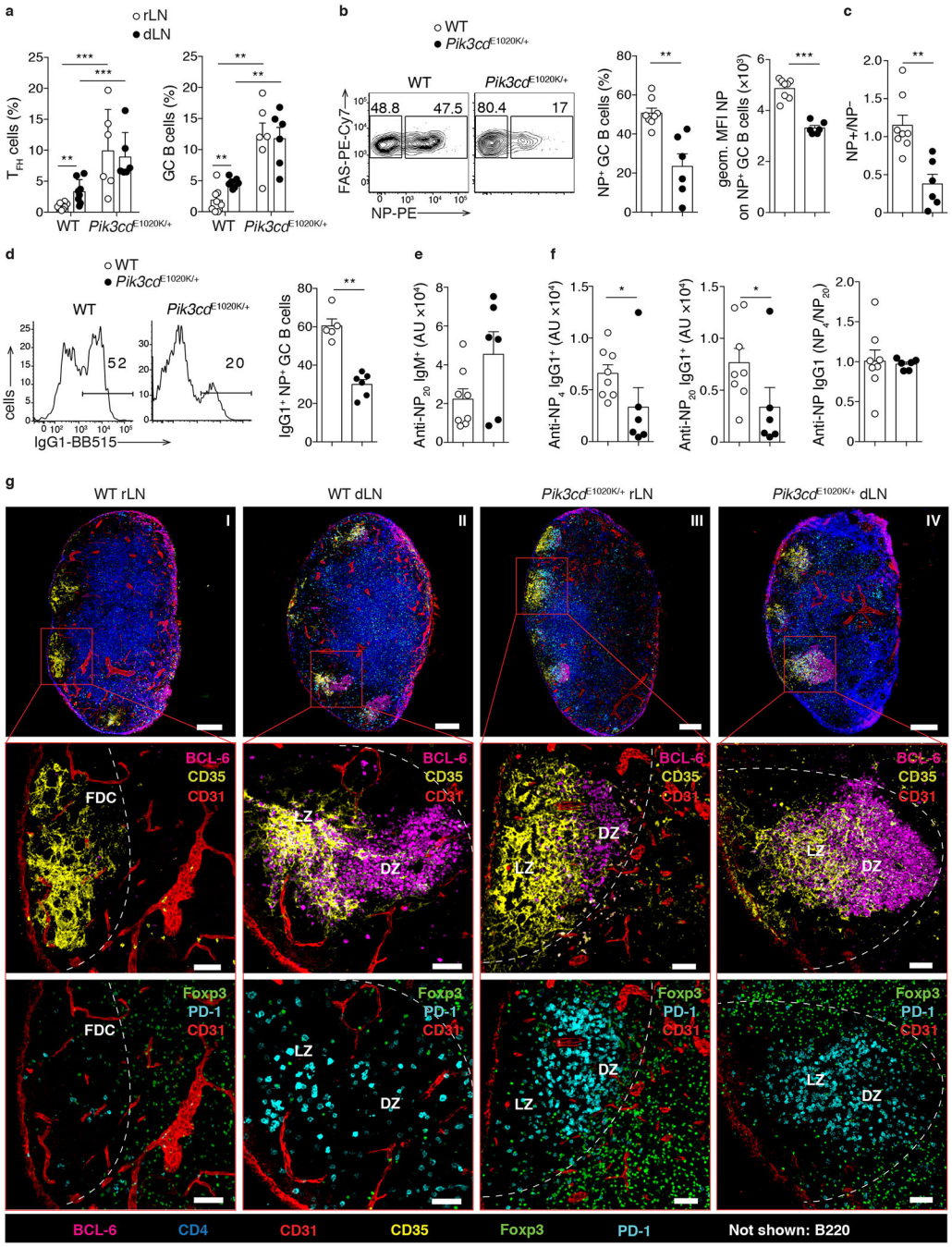

Fig. 3. Defective humoral responses and disorganized GCs in *Pik3cd*$^{E1020K/+}$ mice.

(**a-g**) 4-month-old wild-type and *Pik3cd*$^{E1020K/+}$ mice were immunized s.c. with NP-OVA in alum, and draining (dLN) and resting (rLN) popliteal lymph nodes analyzed on day +10. **a**, Frequency of PD-1^{+}CXCR5^{+}Foxp3$^{—}$ T_{FH} cells (percent of CD4^{+}B220$^{—}$ T cells) and GL-7^{+}FAS^{+} GC B cells (percent of B220^{+}CD19^{+} B cells) in rLN and dLN. **b**, Representative contour plots and histograms of NP^{+} antigen-specific GC B cells (of GC B cells) and geometric MFI of NP binding (on NP^{+} GC B cells) in dLN. **c**, Ratios between numbers of NP^{+} and NP$^{—}$ GC B cells in dLN. **d**, Representative IgG1 staining on NP^{+} GC

B cells in dLN and relative histogram. **e**, Quantification of total (anti-NP_{20}-BSA) IgM serum antibodies. **f**, Quantification of high-affinity (anti-NP_4-BSA) and total (anti-NP_{20}-BSA) NP-specific IgG1 serum antibodies determined by ELISA. On the right, ratios between high-affinity and total NP-specific IgG1 antibodies are shown. (**a-c,e,f**, wild-type n=8, *Pik3cd*$^{E1020K/+}$ n=6; **d**, wild-type n=5, *Pik3cd*$^{E1020K/+}$ n=6). **g**, Immunofluorescence (IF) staining of frozen sections prepared from popliteal rLN and dLN and processed for confocal microscopy. Staining panels are displayed at the bottom. White dotted line corresponds to the boundary between the B cell follicle and T cell zone and is based on B220 staining (not shown). LZ denotes light zone marked by CD35 staining; GCs denoted by BCL-6. IF analyses are representative of 2–3 independent lymph nodes analyzed (scale bar 200 μm, top; 50 μm middle and bottom). Data in (**a-f**) are representative of two independent experiments and are represented as mean ± SEM with each dot indicating one mouse. Significance analyzed by Mann-Whitney U test. *$P < 0.05$; **$P < 0.01$; ***$P < 0.001$.

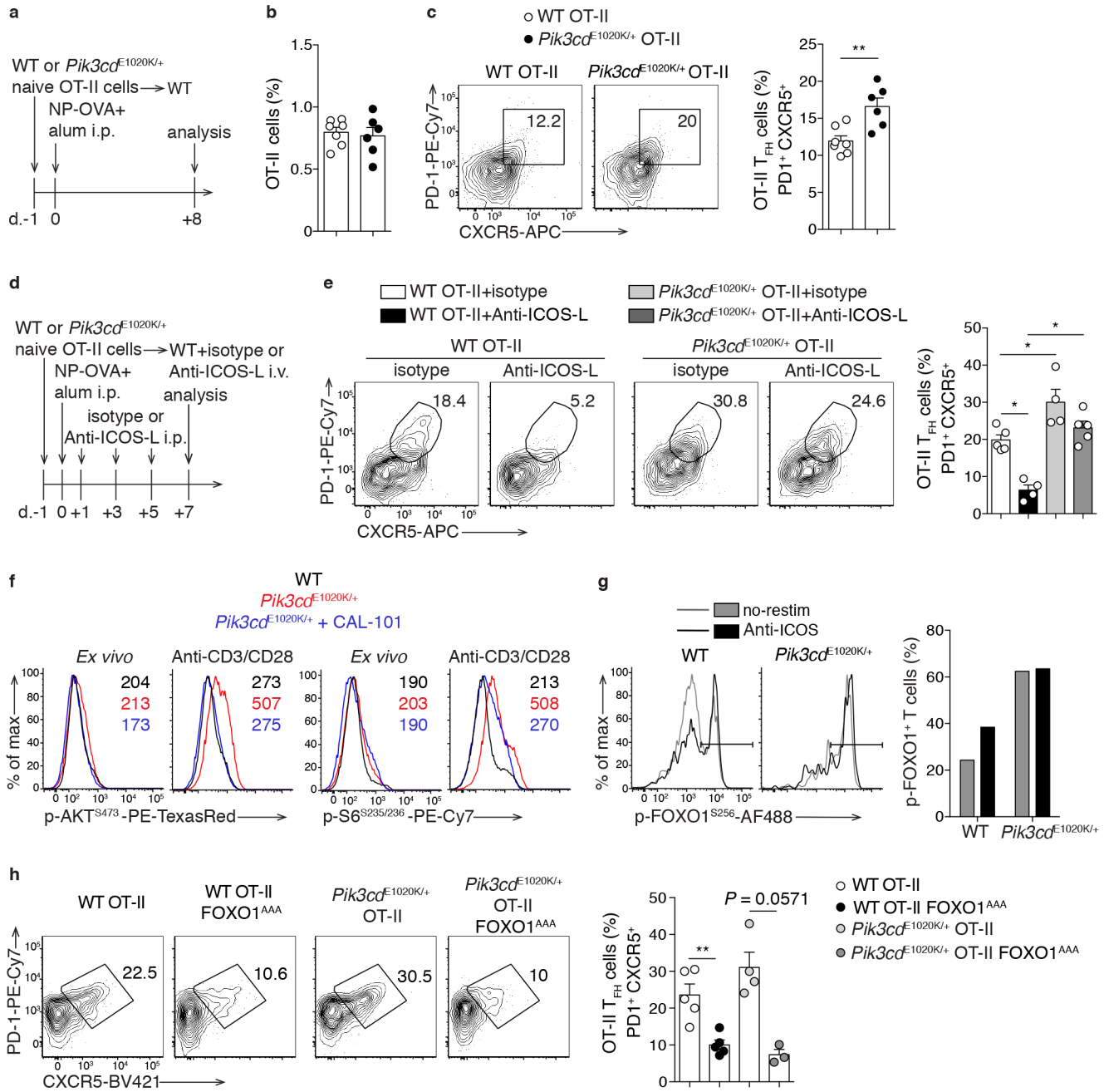

Fig. 4. *Pik3cd*$^{E1020K/+}$ T cells intrinsically generate more T_{FH} cells in ICOS independent manner.

a, Outline for (**b-c**). Wild-type mice (CD45.1$^+$) were transferred with CD45.2$^+$ wild-type (n=7) or *Pik3cd*$^{E1020K/+}$ OT-II cells (n=6), followed by i.p. immunization with NP-OVA in alum. Day+8 analyses of spleens. **b**, Percentage of CD45.2$^+$ OT-II cells in live cells. **c**, Flow plots and summary histogram of percentage of PD-1$^+$CXCR5$^+$ OT-II T_{FH} cells (of OT-II cells). **d**, Outline of anti-ICOS-L *in vivo* treatment: wild-type or mutant OT-II cells were transferred into wild-type hosts, then immunized as in (**a**). Mice received isotype control (wild-type OT-II n=5, *Pik3cd*$^{E1020K/+}$ OT-II n=4), or anti-ICOS-L (wild-type OT-II n=4,

Pik3cd$^{E1020K/+}$ OT-II n=5) on day −1 (i.v.), +1, +3, +5 (i.p.) and were sacrificed on day+7. **e**, Frequency of PD-1^{+}CXCR5^{+} OT-II T_{FH} cells: flow plots and summary histogram. **f**, p-AKT^{Ser473} and p-S6$^{Ser235/236}$ on naïve CD4^{+} T cells *ex vivo* or after 30 min stimulation with anti-CD3 and anti-CD28, after pretreatment with CAL-101 (PI3Kδ inhibitor), or vehicle. Geom. MFI are indicated. **g**, FACS plots and histograms of p-FOXO1^{Ser256} on day+4 *in vitro* activated wild-type and *Pik3cd*$^{E1020K/+}$ CD4^{+} T cells, rested for 1 h in RPMI, then stimulated with anti-ICOS or left untreated (**f,g**, cells pooled from 2–4 mice per group). **h**, FACS plots and histogram of percentages of splenic T_{FH} PD-1^{+}CXCR5^{+} from wild-type (n=5) or *Pik3cd*$^{E1020K/+}$ OT-II cells (n=4) (gated on transduced GFP^{+} cells), and wild-type (n=5) or *Pik3cd*$^{E1020K/+}$ FOXO1^{AAA} OT-II (n=3) cells (gated on transduced GFP^{+} HA^{+} cells), transferred into wild-type hosts, and analyzed day+5 post i.p. immunization with NP-OVA. Data are representative of three (**a-c, g**) and two (**d, e, f, h**) independent experiments. Data in (**b, c, e, h)** are expressed as mean ± SEM with each dot indicating one mouse. Significance analyzed by Mann-Whitney U test. *$P < 0.05$; **$P < 0.01$.

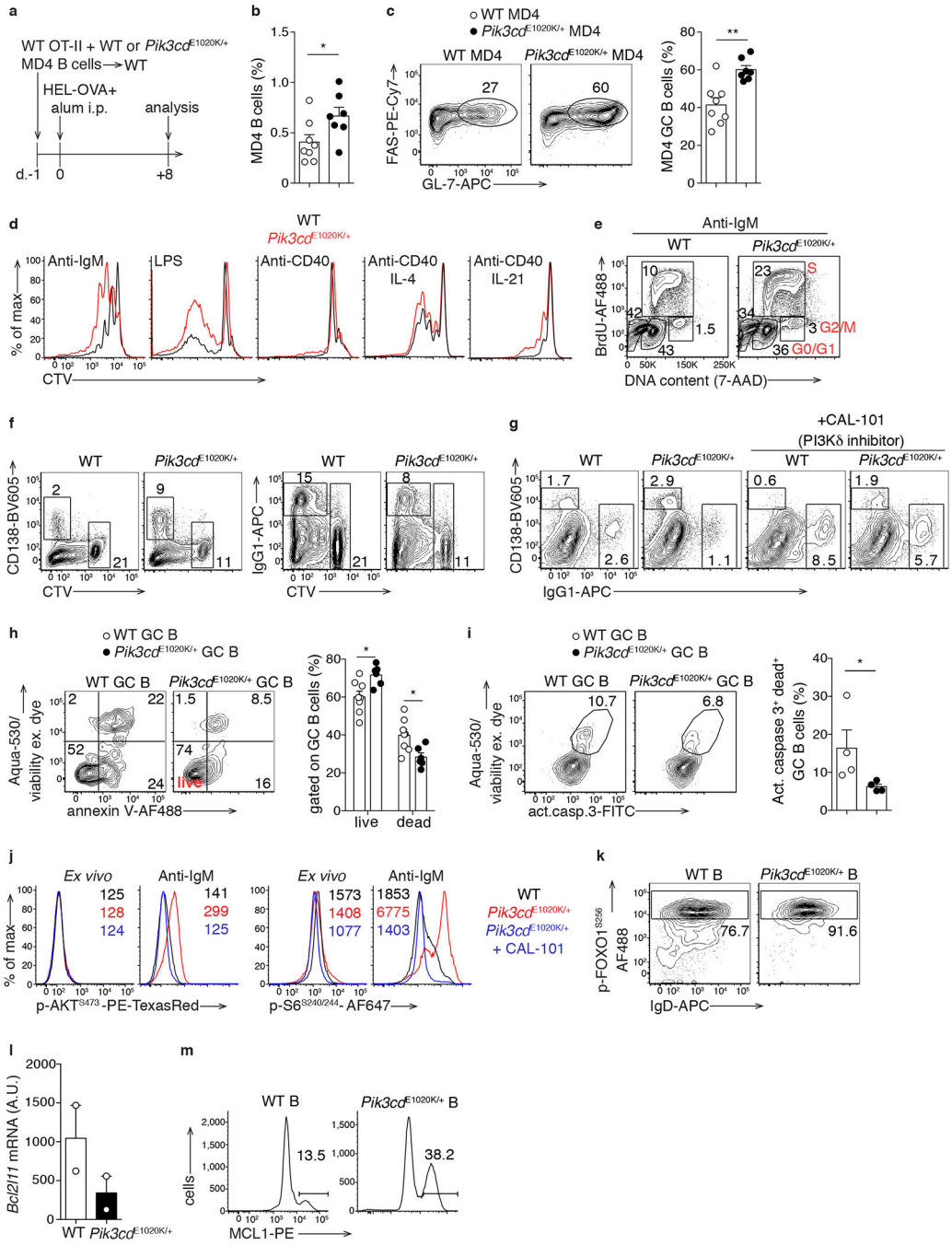

Fig. 5. B cell intrinsic increases in GC B cells with higher proliferation and survival.

a, Outline for (**b, c**). Wild-type OT-II (CD45.1/2$^+$) and wild-type (n=8) or *Pik3cd*$^{E1020K/+}$ (n=7) MD4 B cells (CD45.2$^+$) were transferred in wild-type hosts (CD45.1$^+$), which were then immunized i.p. with HEL-OVA$_{323–339}$. Day+8 analyses of spleens. **b**, Frequency of MD4 B cells in live cells. **c**, Representative contour plots and histogram of MD4 GC B cells (B220$^+$CD19$^+$FAS$^+$GL-7$^+$). **d**, CTV dilution of follicular (FO) B cells activated *in vitro* for 3 days with indicated stimuli (gated on live cells). **e**, BrdU incorporation of FO B cells activated *in vitro* 2 days with anti-IgM. **f**, FO B cells stimulated 3 days with LPS+IL-4 and

analyzed for $CD138^+$ plasma cells (left) and IgG1 switching (right) versus CTV (gated on live cells). **g**, FO B cells stimulated as in (**f**) +/− CAL-101 (live cell gate). **d-g**, 2–4 mice pooled per group. **h**, Representative contour plots of viability-exclusion dye and Annexin V on splenic GC B cells ($B220^+CD19^+FAS^+GL\text{-}7^+$) and histogram of percent live and dead cells (wild-type n=8; *Pik3cd*$^{E1020K/+}$ n=6). **i**, Contour plots and bar graph of viability-exclusion dye and activated caspase-3 on GC B cells as described in (**h**) (n=4 per group). **j**, FACS histograms of p-AKT^{Ser473} and p-S6$^{Ser240/244}$ on naïve FO cells *ex vivo* or after 60 min stimulation with anti-IgM, after pre-treatment with CAL-101 or vehicle (geom. MFIs indicated). **k**, Representative FACS plots of IgD and p-FOXO1^{Ser256} on *in vitro* activated (anti-CD40+IL-4) FO B cells (day+3.5 analysis, gated on $CTV^{—}$ live cells). **j-k**, 2–4 mice pooled per group. **l**, *Bcl2l11* mRNA expression levels from splenic GC B cells, day+7 post i.p. NP-OVA immunization (2 mice pooled per group). **m**, MCL-1 expression on day +3.5 *in vitro* activated (LPS+IL-21) FO B cells, gated on live cells (2–4 mice pooled per group). Data in (**a-c)** pooled from 2 independent experiments; data in (**d-h, l, m)** representative of 3 independent experiments; data in (**i-k)** representative of 2 independent experiments. Data in (**b-c, h, i, l)** are expressed as mean ± SEM with each dot indicating one mouse. Significance analyzed by Mann-Whitney U test. $*P < 0.05$; $**P < 0.01$.

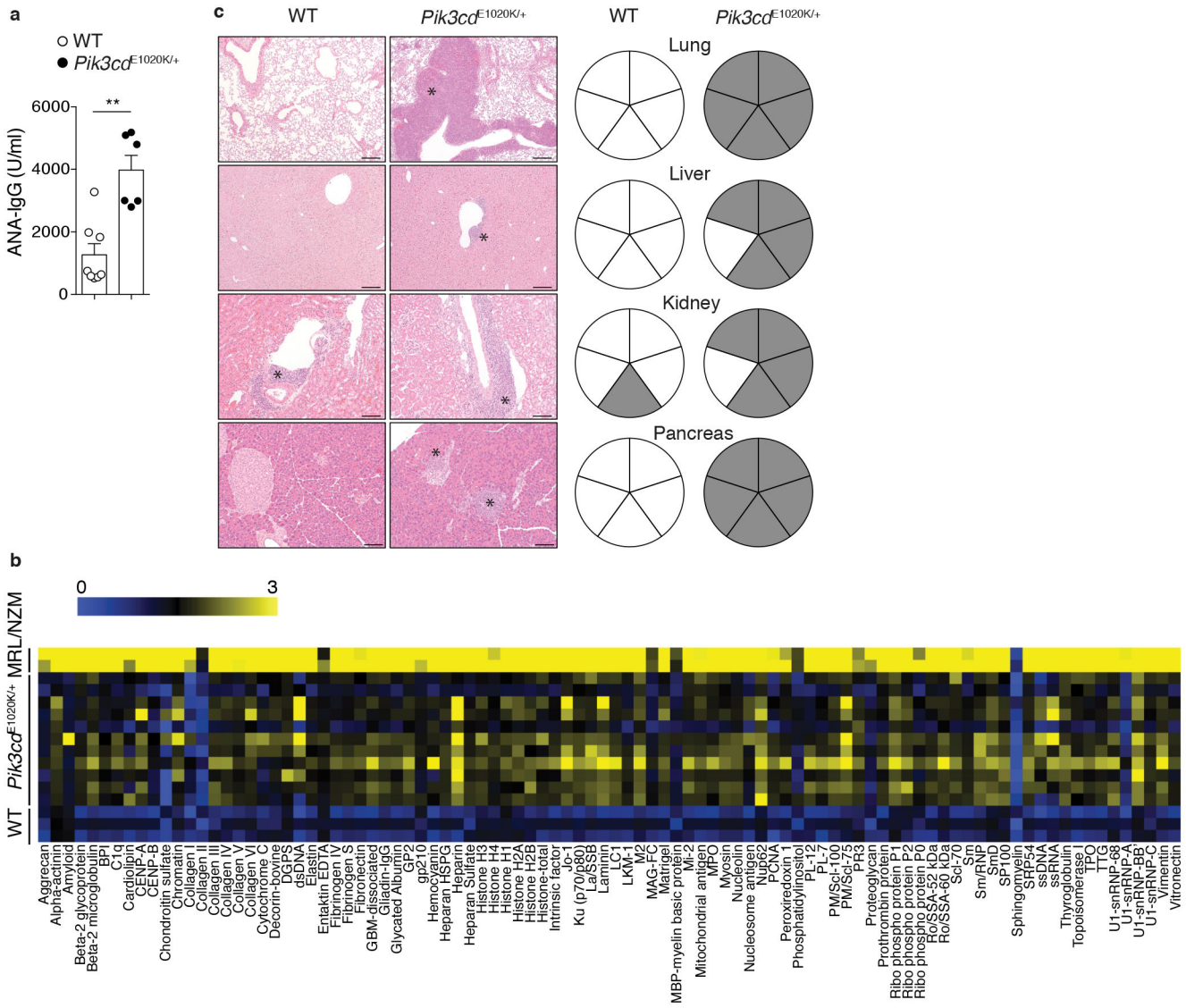

Fig. 6. *Pik3cd*$^{E1020K/+}$ mice develop autoantibodies and infiltration of multiple organs.

a, ELISA for serum ANA-IgG on 14/16-week-old wild-type (n=8) and *Pik3cd*$^{E1020K/+}$ (n=6) mice. **b**, Serum IgG autoantibody array chip is shown; a colorimetric representation of relative autoantibody reactivity is shown based on 0–3 scale. Sera from 3 wild-type, 11 *Pik3cd*$^{E1020K/+}$ and 2 lupus-prone positive control MRL/NZM mice were analyzed **c**, H&E staining of perfused lung, liver, kidney, pancreas from 14-month-old wild-type and *Pik3cd*$^{E1020K/+}$ mice at steady state. Cell infiltrations are indicated with asterisks. Right, pie charts with each segment representing one mouse; grey denotes cell infiltration into the organs (scale bar 200 μm, lung and liver; 100 μm, kidney and pancreas) (n=5 per group). Data in (**a**) are representative of 3 independent experiments. Data in (**b**) were obtained from one experiment analyzing mice from multiple litters. Data in (**c**) were representative of 2 independent experiments. Data in (**a**) are expressed as mean ± SEM with each dot indicating one mouse Significance analyzed by Mann-Whitney U test. ** $P < 0.01$.

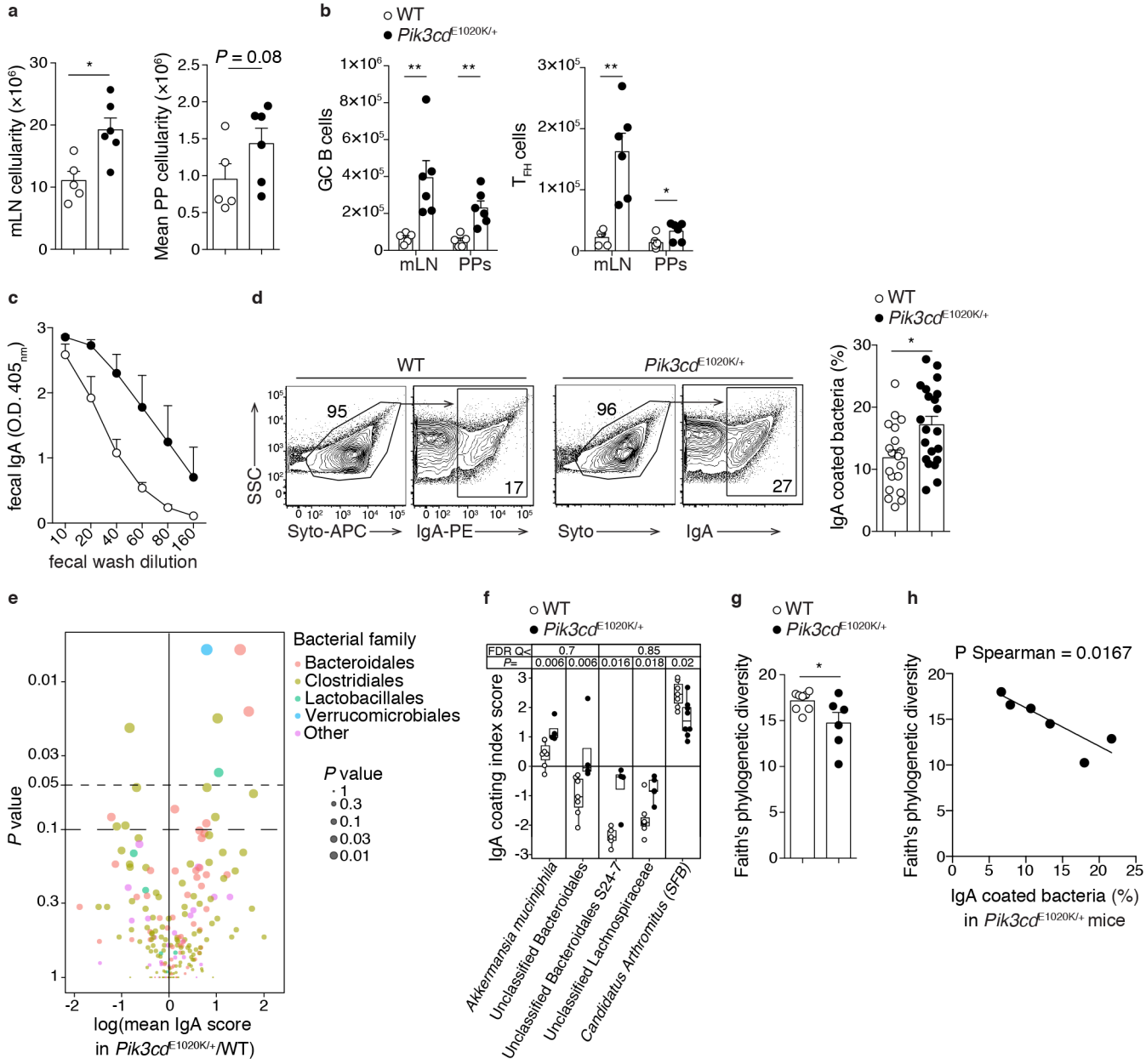

Fig. 7. Altered homeostasis of GALT with increased IgA coated fecal bacteria in *Pik3cd*$^{E1020K/+}$ mice.

(**a-h**) Analysis of 10–12-week-old naïve wild-type and *Pik3cd*$^{E1020K/+}$ mice. **a**, Cellularity of mesenteric LN (mLN) and Peyer's patches (PPs). **b**, Numbers of GC B cells ($B220^+CD19^+GL\text{-}7^+FAS^+$) and T_{FH} cells ($CD4^+B220^-PD\text{-}1^+CXCR5^+Foxp3^-$) in mLN and PPs (wild-type n=5, *Pik3cd*$^{E1020K/+}$ n=6). **c**, IgA ELISA on fecal wash (n=3 per group). **d**, Representative contour plots for fecal bacteria ($Syto^+$) and percentage of IgA-coated bacteria; right, summary histograms of percentages of IgA-coated bacteria (wild-type n=19, *Pik3cd*$^{E1020K/+}$ n=21). **e**, Volcano plot of mean fold change IgA scores of coated bacteria in *Pik3cd*$^{E1020K/+}$ versus wild-type mice. **f**, Top bacterial taxa with differential IgA-coating scores in wild-type versus *Pik3cd*$^{E1020K/+}$. Serial Mann-Whitney U tests were performed on

all taxa that were detected in at least four mice from each group and Benjamini-Hochberg q values were calculated (**e, f** wild-type n=7, *Pik3cd*$^{E1020K/+}$ n=9). **g**, Faith's phylogenetic alpha diversity in wild-type (n=8) and *Pik3cd*$^{E1020K/+}$ (n=6) mice (significance analyzed by Unpaired t test). **h**, Correlation between alpha diversity and overall percentage of IgA-coated fecal bacteria in *Pik3cd*$^{E1020K/+}$ (n=6). Data are representative of 3 independent experiments (**a-c, e-h**). Data in (**d**) are pooled from 5 independent experiments. Data in (**a-d, g**) are expressed as mean ± SEM with each dot indicating one mouse. Significance in (**a, b, d**) analyzed by Mann-Whitney U test. *$P < 0.05$; **$P < 0.01$; ***$P < 0.001$.

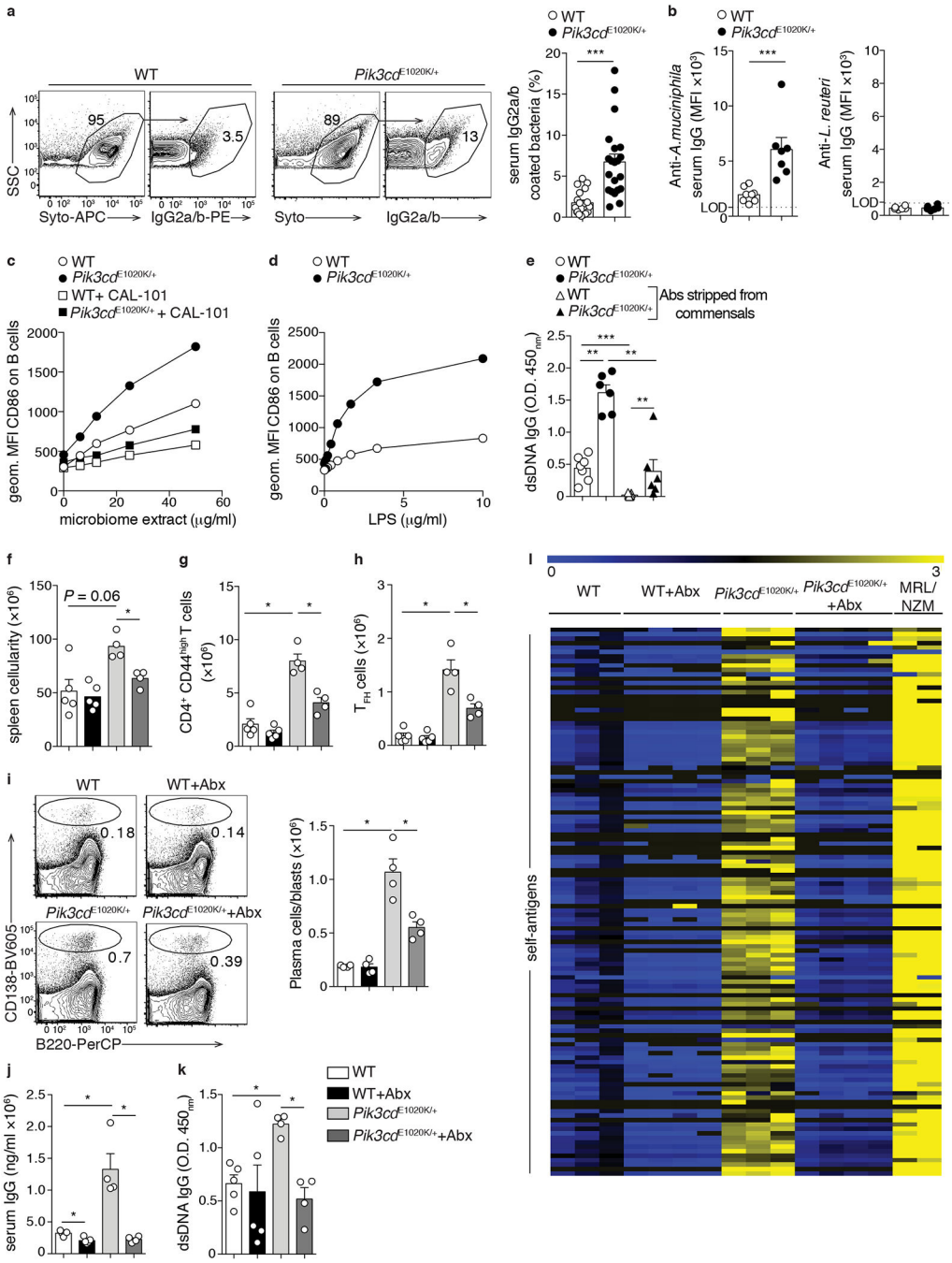

Fig. 8. Increased commensal reactivity and reduced activated phenotypes after antibiotic treatment in *Pik3cd*$^{E1020K/+}$ mice.

a, Contour plots of fecal bacteria (Syto^{+}) and serum IgG2a/b (detects IgG2c/b-binding in C57BL/6 mice) binding fecal bacteria. Histograms indicate percentage of serum IgG2a/b-coated bacteria (wild-type n=19, *Pik3cd*$^{E1020K/+}$ n=21). **b**, MFI of *A. muciniphila* and *L. reuteri* bound by serum IgG (wild-type n=8, *Pik3cd*$^{E1020K/+}$ n=7). **c-d**, CD86 MFI on splenic naïve follicular (FO) B cells after 20 h *in vitro* stimulation with **c**) autologous fecal bacteria extracts (+/− CAL-101), or **d**) LPS (**c,d** pool of 3 mice per group). **e**, ELISA for dsDNA IgG

on sera and on serum antibodies stripped from commensals obtained as in (**a**) (wild-type n=7, *Pik3cd*$^{E1020K/+}$ n=6). (**f-l**) Littermate wild-type and *Pik3cd*$^{E1020K/+}$ mice were treated for 6 weeks starting at weaning, with antibiotics+sweetener, or sweetener alone (**f-h, j,k** wild-type n=5, *Pik3cd*$^{E1020K/+}$ n=4, for both treatments). **f**, Spleen cellularity. **g**, Numbers of splenic CD44^{hi} CD4^{+} T cells. **h**, Numbers of splenic T_{FH} cells (CD4^{+}B220$^{—}$ PD-1^{+}CXCR5^{+}Foxp3$^{—}$). **i**, Percentages (of live cells) and numbers of splenic plasma cells (CD138^{+}B220$^{int/lo}$) (n=4 per group). **j**, ELISA for serum IgG, and (**k**) for dsDNA IgG. **l**, Serum IgG autoantibody array: colorimetric representation of relative autoantibody reactivity based on 0–3 scale (wild-type n=3, wild-type+Abx n=4, *Pik3cd*$^{E1020K/+}$ n=3, *Pik3cd*$^{E1020K/+}$ +Abx n=4, MRL/NZM n=2). Data in (**a**) are the pool of 5 independent experiments. Data in (**b**) are from one experiment using samples from mice housed in 3–4 independent cages/genotype. Data in (**c-d**) are representative of 2 independent experiments. Data in (**e-k**) are representative of 3 independent experiments. Data in (**l**) were from one experiment. Data in (**a-b, e-k**) are expressed as mean ± SEM with each dot indicating one mouse. Significance analyzed by Mann-Whitney U test. *$P < 0.05$; **$P < 0.01$; ***$P < 0.001$.